Master's thesis

NTNU
Norwegian University of Science and Technology
Faculty of Natural Sciences
Department of Materials Science and Engineering

Astrid Nordhus

Modelling Gas Flow in Furnaces for Si Production

Master's thesis in Material Science and Engineering
Supervisor: Professor Merete Tangstad
Co-supervisor: Senior Research Scientist Eli Ringdalen
January 2022

NTNU
Norwegian University of
Science and Technology

Astrid Nordhus

Modelling Gas Flow in Furnaces for Si Production

Master's thesis in Material Science and Engineering
Supervisor: Professor Merete Tangstad
Co-supervisor: Senior Research Scientist Eli Ringdalen
January 2022

Norwegian University of Science and Technology
Faculty of Natural Sciences
Department of Materials Science and Engineering

NTNU
Norwegian University of
Science and Technology

Preface

This report is the evaluation basis for the course TMT4905 – Materials Science, Master's thesis at the Norwegian University of Science and Technology. The work was performed at the Department of Material Science and Engineering as a part of the project Reduced energy consumption by increased reduction volume, KPN ReCursive, RCN project number 326581 founded by the Research Council of Norway (RCN) and The Norwegian Ferroalloy Producers Research Association (FFF).

The thesis describes an investigation of the effect particle size, temperature, and gas velocity have on the pressure drop in the silicon furnace. To study the pressure-drop, gas flow through porous media was simulated using the software OpenFOAM. This thesis is a continuation of a project work done by the author in the fall of 2021. The results from the project work are submitted and approved for publishing under the title *"Gas flow and pressure drop in charge material in Silicon production"*, in the member journal of The Minerals, Metals & Materials Society, and is ready for publishing in October 2022.

I would like to thank my supervisors Professor Merete Tangstad and Senior Research Scientist Eli Ringdalen at SINTEF for giving me the opportunity to write this project. I want to give a special thanks to Eli Ringdalen for helpful discussions, guidance, and feedback in addition to having confidence in me allowing me to shape the task and choosing the direction of the investigations. I would also like to thank Professor Kristian Etienne Einarsrud for all the help and guidance with OpenFOAM, and in getting the simulation to work.

Abstract

For the silicon industry, important goals are lower energy consumption and higher silicon yield. To achieve this, it is important that the processes in the furnace are stable. Increased pressure in the furnace from the process gases could cause operational problems. A better understanding of what affects the pressure and the gas flow in the furnace is thus of importance.

The objective of this work has been to investigate how the particle sizes of the raw materials affect the pressure-drop in furnaces for silicon production. The effect of gas velocity and temperature has also been studied. Two models have been developed for simulating the pressure-drop through the charge material in silicon furnaces, one with incompressible gas flow meaning that the density is assumed constant, and one with compressible gas flow.

The particle size of quartz was found to be the most important of the parameters studied regarding the build-up of pressure in the furnace, where quartz with particle sizes below 2.00 mm showed a significant rise in pressure for all temperatures and velocities studied. Quartz above 2.00 mm was found to have a low effect on pressure. Higher velocities resulted in higher pressures. When velocity was kept constant a rise in temperature showed the opposite effect resulting in a somewhat lower build-up of pressure. However, as a rise in temperature causes a rise in velocity, a rise in temperature generally results in a rise in pressure.

Sammendrag

Lavere energiforbruk og høyere silisium utbytte er viktig for silisium produksjonen. For å oppnå dette er det viktig med stabile ovnsprosesser. Motstand mot gass-strømning i råmaterialet fører til et økt trykk i ovnen. Om dette trykket blir for høyt kan det føre til ulike driftsproblemer. Det er derfor viktig med en god forståelse av hva som påvirker trykket og gass-strømningen i ovnen.

Målet med dette arbeidet har vært å undersøke hvordan partikkelstørrelsen på råmaterialet påvirker trykket i en silisium-ovn. Hvordan gass hastigheten og temperaturen påvirker trykket er også studert. To ulike modeller har blitt utviklet for å simulere trykket og gass-strømningen i ovnen. En av modellene antar inkompressibel strømning, altså at gassen har konstant tetthet, mens den andre modellen antar kompressibel strømning.

Av faktorene studert i denne oppgaven hadde partikkelstørrelsen størst effekt på trykket. Kvarts med partikkelstørrelse under 2.00 mm medførte et høyt trykk for alle temperaturer og gass hastigheter undersøkt. Kvarts med partikkelstørrelser over 2.00 mm hadde derimot liten effekt på trykket. Høyere hastighet medførte høyere trykk. Om hastigheten ble holdt konstant viste temperaturen en motsatt effekt hvor høyere temperatur medførte et noe lavere trykk. I og med at en økning i temperatur medfører en økning i hastighet vil derimot økt temperatur generelt sett medføre et høyere trykk.

Contents

Preface i
Abstract iii
Sammendrag v
Contents vii
List of Figures x
List of Tables xv
List of Symbols and Abbreviations xvii
1 Introduction 1
1.1 Background 1
1.2 Objective 3
2 Literature Review 5
2.1 Metallurgical Production of Silicon 5
2.1.1 Chemical Reactions in the Furnace 5
2.1.2 Thermodynamics of the System 7
2.1.3 Energy Consumption and Silicon Yield 9
2.2 Permeability of Charge Mixtures 10
2.2.1 Formation of Fines and Clogging 11
2.2.2 Condensate Formation 12
2.3 Different Zones in the Furnace 13
2.3.1 Excavations of Si Furnaces 13
2.4 Furnace Crater Pressure 16
2.5 Gas Flow Through Porous Media 19
2.5.1 Pressure-Drop in Packed Beds 19
2.5.2 General Description of Fluid Flow 21
2.6 Measurements of Pressure Through Charge 23

2.7 Simulating Fluid Flow Using CFD in OpenFOAM 29
2.7.1 Solvers for Flow Through Porous Media 29
2.7.2 File Structure in OpenFOAM Cases 31
3 Methodology 35
3.1 Choice of Cases and Parameters 35
3.2 Geometry for Simulations of Gas Flow in an Industrial Furnace 37
3.3 Calculation of Gas Volumes and Gas Velocities 38
3.4 Modelling 39
3.4.1 Base Cases 39
3.4.2 Parameters Set for the Simulations 40
3.4.3 Simulating Small-Scale Cold Experiment 43
3.4.4 Up-Scaling of Model to Simulate Furnace Conditions 45
4 Results 49
4.1 Pressure-Drop at Furnace Conditions at Different Temperatures 49
4.2 Pressure-Drop at Furnace Conditions with Varying Velocity 52
4.3 Pressure Across the Simulated Area 54
4.4 Velocity Across the Simulated Area 57
4.5 Simulations of Small-Scale Cold Experiments 60
5 Discussion 61
5.1 Effect of Particle Size 61
5.2 Effect of Temperature and Gas Velocity 63
5.3 Validation of Models 65
5.4 Comparison of the Two Models Used 68
5.5 Pressure-Drop in Industrial Furnaces 71
6 Conclusion 73
7 References 75
Appendix 79

A Result from Simulations 79

B Geometry of Up-Scaled Simulations with Furnace Conditions 81

C Geometry of Small-Scale Cold Experiment 83

List of Figures

Figure 1.1: A typical plant for production of metallurgical silicon. The figure is reprinted from Schei et al [1]. 2

Figure 2.1: Illustration of the inner structure of a Si furnace with reactions taking place. Figure from [12]. 7

Figure 2.2: Equilibrium diagram for the SiO pressure above the condensed phase combinations C-SiC, SiO_2-C, SiO_2-SiC, SiC-Si, and SiO_2-Si as illustrated by Schei et al [1]. The total pressure is assumed to be 1 bar consisting of only SiO gas and CO gas. 9

Figure 2.3: Illustration of gas flow in a charge with a low amount of fines (left) and a high amount of fines (right) [18]. 11

Figure 2.4: Overview of the zones in the furnace around the electrodes from an excavation of a ferrosilicon furnace at Finnfjord [22]. 14

Figure 2.5: Overview of the different zones found from the excavation of three different Si furnaces: a) Wacker furnace no. 1, b) Elkem Thamshavn, c) Wacker furnace no. 4 [25]. 15

Figure 2.6: Crater pressure and electrode load measured at furnace 2 at Elkem Thamshavn [15] 17

Figure 2.7: Measurements of pressure at different electrodes in the furnace compared with stoking (blue line), % dust (black line) and temperature (red line) under continuous feeding of raw materials [28]. 17

Figure 2.8: 2D contours of simulated pressure pattern around two electrodes above the melt in the silicon furnace [29]. 18

Figure 2.9: Simulated pressure drop from gas flow in a 40 MW silicon furnace for different particle sizes plotted as a function of particle sphericity. The dotted black line show a basis pressure in an industrial furnace [17]. 19

Figure 2.10: A schematic representation of the pressure drop apparatus. Illustration from [5]. 24

Figure 2.11: Estimated pressure for the packed beds with a homogeneous mixture of coal and quartz with and without woodchips. The regression is estimated from data from

the pressure sensor at the lowest position. The continuous line represents Run 1 and the truncated line represents Run 2 [8]. 25

Figure 2.12: Estimated regression line for the pressure drop as a function of velocity for the packed bed containing woodchips, unsieved coal, and quartz at 2.00 – 4.75 mm. The indicators show the average pressure values at a given velocity and the dotted lines show a 95 % confidence interval for the regression line. 26

Figure 2.13: Estimated regression lines for the pressure drop as a function of velocity for all size fractions of coal with quartz at the size fraction 0.25 – 2.00 mm. The indicators show the average pressure values at a given velocity and the dotted lines show a 95 % confidence interval for the regression line of the corresponding color [6]. 27

Figure 2.14: Estimated regression lines for the pressure drop as a function of velocity for all size fractions of coal with quartz at the size fraction 2.00 – 4.75 mm. The indicators show the average pressure values at a given velocity and the dotted lines show a 95 % confidence interval for the regression line of the corresponding color [6]. 27

Figure 2.15: Estimated regression lines for the pressure drop as a function of velocity for all size fractions of coal with quartz at the size fraction 4.75 – 10.00 mm. The indicators show the average pressure values at a given velocity and the dotted lines show a 95 % confidence interval for the regression line of the corresponding color [6]. 28

Figure 2.16: Files in the porousSimpleFoam solver. 30

Figure 2.17 Case directory structure in OpenFOAM. Picture from [43]. 31

Figure 2.18: Case structure of the tutorial case for the porousSimpleFoam solver. 32

Figure 2.19: Case structure for the tutorial case for the rhoPorousSimpleFoam solver. 33

Figure 3.1: The area of charge material that is the basis for the geometry of the simulation is highlighted by the red dotted lines. 37

Figure 3.2: a) Geometry of the case for the small-scale cold experiment. b) section of the lower part of the geometry enlarged to show the meshing..... 44

Figure 3.3: Geometry of the cases for the up-scaled furnace conditions. 46

Figure 3.4: Meshing of the cases for the up-scaled furnace conditions. 46

Figure 4.1: Pressure in kPa from simulations with incompressible flow for the three cases at different temperatures. The green indicators represent Case 1 (quartz at 0.25 – 2.00 mm and coal at 2.00 – 3.35 mm) with the lowest permeability, the red indicators represent Case 2 (quartz at 2.00 – 4.75 mm and coal 5.00 – 10 mm) with higher permeability, and the blue indicators represents Case 3 (quartz at 2.00 – 4.75 mm, coal below 10 mm, and woodchips at 2 – 5 cm) with the highest permeability. 50

Figure 4.2: Pressure in kPa from simulations with compressible gas flow for the three cases at different temperatures. The green indicators represent Case 1 (quartz at 0.25 – 2.00 mm and coal at 2.00 – 3.35 mm) with the lowest permeability, the red indicators represent Case 2 (quartz at 2.00 – 4.75 mm and coal 5.00 – 10 mm) with higher permeability, and the blue indicators represents Case 3 (quartz at 2.00 – 4.75 mm, coal below 10 mm, and woodchips at 2 – 5 cm) with the highest permeability. 51

Figure 4.3: Pressure in kPa from simulations with incompressible gas flow and permeability of Case 2 with quartz at 2.00 – 4.75 mm and coal at 5.00 – 10 mm. The green indicators show the pressure from simulations at 1400 °C at different velocities. 52

Figure 4.4: Pressure in kPa from simulations with compressible gas flow and permeability of Case 2 with quartz at 2.00 – 4.75 mm and coal at 5.00 – 10 mm. The green indicators show the pressure from simulations at 1400 °C at different velocities. 53

Figure 4.5: Pressure fields from the simulations of Case 1 at 1750 °C with a) incompressible gas flow and b) compressible gas flow. 54

Figure 4.6: Pressure in kPa plotted against the height of the simulated area in m from the simulation of Case 1 at 1750 °C with incompressible gas flow. 55

Figure 4.7: Pressure plotted against the height of the simulated area from the simulation of Case 1 at 1750 °C with compressible gas flow. 56

Figure 4.8: Velocity plotted against the height of the simulated area from the simulation of Case 1 at 1750 °C with incompressible gas flow. 57

Figure 4.9: Velocity plotted against the height of the simulated area from the simulation of Case 1 at 1750 °C with compressible gas flow. 58

Figure 4.10: Pressures in kPa from the simulations of the small-scale cold experiment with incompressible flow. The green indicator represents the simulation of case 1, the red indicator represents case 2, and the blue indicator represents case 3. 60

Figure 4.11: Pressures in kPa from the simulations of the small-scale cold experiment with compressible flow. The green indicator represents the simulation of case 1, the red indicator represents case 2, and the blue indicator represents case 3. 60

Figure 5.1: Pressure in kPa from Case 2 with quartz at 2.00 – 4.75 mm and coal at 5.00 – 10 mm, and Case 3 with quartz at 2.00 – 4.75 mm, coal below 10 mm, and woodchips at 2 – 5 cm, at different temperatures simulated with incompressible flow. 62

Figure 5.2: Pressure in kPa from Case 2 with quartz at 2.00 – 4.75 mm and coal at 5.00 – 10 mm, and Case 3 with quartz at 2.00 – 4.75 mm, coal below 10 mm, and woodchips at 2 – 5 cm, at different temperatures simulated with compressible gas flow. 62

Figure 5.3: Pressure in kPa from simulations with incompressible gas flow and permeability of Case 2 with quartz at 2.00 – 4.75 mm and coal at 5.00 – 10 mm. The green indicators show the pressures at 1400 °C, the blue indicator show the pressure from the simulation at 700 °C, and the red indicator show the pressure from the simulation at 1750 °C. 63

Figure 5.4: Pressure in kPa from simulations with compressible gas flow and permeability of Case 2 with quartz at 2.00 – 4.75 mm and coal at 5.00 – 10 mm. The green indicators show the pressures at 1400 °C, the blue indicator show the pressure from the simulation at 700 °C, and the red indicator show the pressure from the simulation at 1750 °C. 64

Figure 5.5: The indicators show the pressures from the incompressible (blue) and compressible (red) simulations for Case 1 with quartz at 0.25 – 2.00 mm and coal at 2.00 – 3.35 mm. The green solid line shows the estimated regression line from previous experimental work. The dotted lines show a 95 % confidence interval for the calculated regression line [6]. 66

Figure 5.6: The indicators show the pressures from the incompressible (blue) and compressible (red) simulations for Case 2 with quartz at 2.00 – 4.75 mm and coal at 5.00 – 10 mm. The green solid line shows the estimated regression line from previous experimental work. The dotted lines show a 95 % confidence interval for the calculated regression line [6]. 66

Figure 5.7: The indicators show the pressures from the incompressible (blue) and compressible (red) simulations for Case 3 with quartz at 2.00 – 4.75 mm, coal below 10 mm, and woodchips at 2 – 5 cm. The green solid line shows the estimated regression

line from previous experimental work. The dotted lines show a 95 % confidence interval for the calculated regression line [8]. 67

Figure 5.8: Pressures from simulation of packed beds with quartz at 0.25 – 2.00 mm and coal at 2.00 – 3.35 mm (Case 1). The red indicators represent the incompressible solutions, and the blue indicators represent the compressible solutions. 69

Figure 5.9: Pressures from simulation of packed beds with quartz at 2.00 – 4.75 mm and coal at 5.00 – 10 mm (Case 2), and quartz at 2.00 – 4.75 mm, coal below 10 mm, and woodchips at 2 – 5 cm (Case 3). The blue indicators represent the incompressible solutions, and the red indicators represent the compressible solutions. The triangular points are the pressures from Case 2 and the circular points are the pressures from Case 3..... 70

List of Tables

Table 2.1: Size fractions used for quartz and coal [6]. 23

Table 2.2: Calculated values for the Darcy-Forchheimer coefficients D and F [6], [8]. 28

Table 3.1: Description of the three cases studied with material sizes and the Darcy-Forchheimer coefficients D and F. 36

Table 3.2: Mass CO gas and SiO gas produced per hour in a 45 MW furnace [45]. 38

Table 3.3: Gas volume and velocity at different temperatures. 38

Table 3.4: Parameters set in the controlDict for the simulations of both the incompressible and the compressible cases. 40

Table 3.5: Tolerances and relaxation factors used for the simulations. 40

Table 3.6: Initial values for fields that are identical for the incompressible and the compressible solvers. 41

Table 3.7: Initial values for fields that are not identical for the incompressible and the compressible solvers. 41

Table 3.8: Thermodynamic properties of air at 25 °C, 700 °C, 1400 °C, and 1750 °C [47]. ... 42

Table 3.9: Geometry and meshing of the simulations for the small-scale cold experiments. ... 43

Table 3.10: List of simulations for the small-scale cold experiments. All cases were simulated with solvers for both incompressible and compressible gas flow. 44

Table 3.11: Geometry and meshing of the up-scaled simulations. 45

Table 3.12: List of simulations for the up-scaled conditions. All cases were simulated at the temperatures 1750 °C, 1400 °C, and 700 °C, with solvers for both incompressible and compressible gas flow. At 1400 °C the gas velocity was varied. 47

Table 4.1: Velocities from the compressible simulations at the different temperatures for all three cases. 59

Table 4.2: Velocities from the compressible simulations at 1400 °C, where the velocity was varied. 59

Table A.1: All simulations done with upscaled conditions with temperature, solver, case, velocity, and resulting pressure. 79

Table A.2: All simulations done with small-scale conditions corresponding to previous experimental conditions with solver, case, velocity and resulting pressure. 80

List of Symbols and Abbreviations

Symbol	Unit	Description
x	-	Silicon yield
V	m/s	Volumetric flux/ averaged velocity
$\dot{V}_f$	m^3/s	Volumetric flow
A_0	m^2	Area perpendicular to fluid flow
P	Pa	Pressure
L	m	Height of packed bed
ε	-	Void fraction
φ	-	Particle sphericity
d_p	m	Particle diameter
ρ	kg/m^3	density of fluid
μ	kg/ms	dynamic viscosity of fluid
k_1	-	Darcy coefficient
k_2	m	Forchheimer coefficient
D	-	Adjusted Darcy coefficient
F	m^{-1}	Adjusted Forchheimer coefficient
$\boldsymbol{u}$	m/s	Velocity vector
τ	N/m^2	Stress tensor
T	$K/$ ℃	Temperature

Abbreviations

SAF	Submerged Arc Furnace
CFD	Computational Fluid Dynamics
RAM	Random access memory
CPU	Central Processing Unit
RAS	Reynolds Averaged Simulations
2D	two dimensional

1 Introduction

1.1 Background

Silicon is the second most abundant element in the earth's crust after oxygen, where 28 wt% of the earth's crust is estimated to be silicon. In its natural state silicon is almost exclusively bound as silicon dioxide and silicates [1].

Silicon is mostly used as an element for making alloys including aluminium-silicon and ferro-silicon. It is also needed to make silicones [2]. In the electronics industry, silicon is used as a semiconductor. Devices such as transistors, circuit boards, and integrated circuits make use of the conductive properties of silicon to maximize their performance [3]. In addition, silicon is widely used for photovoltaic applications where over 90 % of the world's solar cells are made of silicon [4].

Metallurgical silicon is produced by separating the silicon from the oxygen through a carbothermic reduction of silica, SiO_2, in a submerged arc furnace, SAF. This is a highly energy-intensive process, where a typical plant has an electrical energy consumption of 11 – 13 MWh per metric ton of silicon produced [1]. The main reactants are quartz and carbonous material such as coal, coke, charcoal, and woodchips. The overall idealized reaction can be written:

$$SiO_2 + 2C = Si + 2CO_{(g)} \tag{1.1}$$

A typical silicon production plant is illustrated in Figure 1.1. The raw material is added from the top and descend through the furnace. When it reaches the lower parts of the furnace, where the temperature is 1750 °C and higher, SiO_2 reacts with carbon to form SiO gas and CO gas. These react further to create SiC and Si. Both SiO gas and SiC are necessary as intermediate steps in the production of silicon [1].

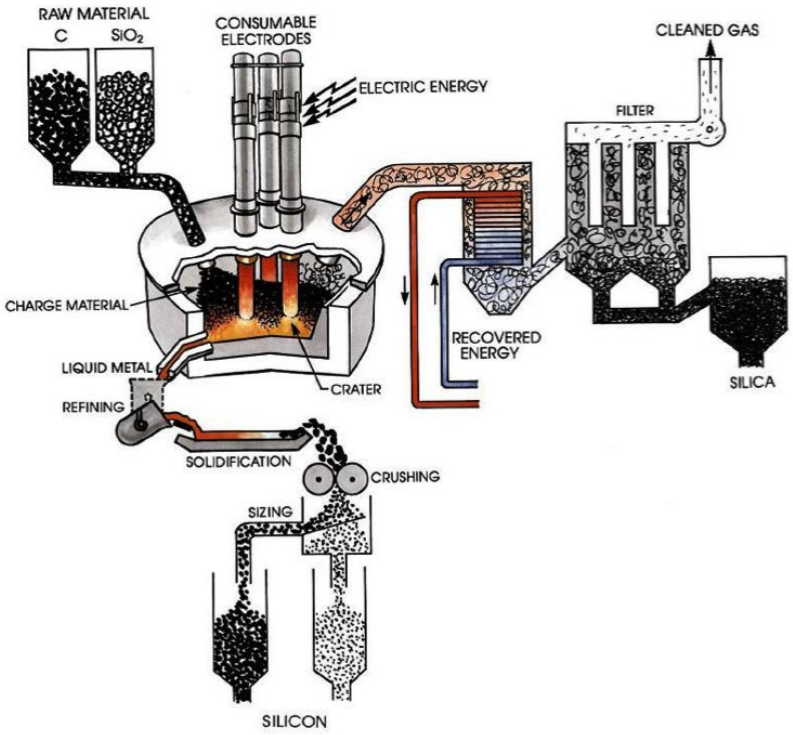

Figure 1.1: A typical plant for production of metallurgical silicon. The figure is reprinted from Schei et al [1].

It is important that as much of the silicon in the SiO gas as possible is retrieved as it rises through the charge material. SiO gas lost to the exhaust system causes both a lower silicon yield and a higher energy consumption per ton silicon produced. Silicon from SiO gas is retrieved as it ascends through the charge material either by reaction with carbon producing SiC or by self-condensation producing Si and SiO_2 [1]. To achieve a high silicon recovery, it is important that the gas containing SiO is allowed to easily rise through the charge and is evenly distributed across the charge material. An evenly distributed gas across the charge material gives a higher contact area with the carbon where the silicon retrieving reactions can occur. As the average velocity of the gas can be found by dividing the volumetric gas flux on the area, an evenly distributed gas will also result in a lower gas velocity compared with gas traveling through narrow channels formed in the charge. With a lower velocity, the gas uses more time to rise through the charge, thus giving longer time for the silicon retrieving reactions to occur [5], [6].

It is important that the processes in the furnace are stable to achieve a lower energy consumption and a higher silicon yield. To get stable processes in the furnace, it is important with an even gas flow. Resistance to gas flow is caused by the permeability of the charge

material. A lower permeability causes a higher resistance to gas flow, which again causes a build-up of pressure from the process gasses. The permeability of the charge is lowered by various reasons including the creation of a dense layer of condensate of Si, SiO_2, and SiC, but also the packing of the raw materials and fines formation which clogs the pores in the structure [6]. An increased pressure may cause different operational problems. Examples of such problems are sudden outbursts of gas and channel formation where the gas no longer is evenly distributed across the charge, resulting in a lower recovery of silicon from SiO. This causes more silicon to be lost in the off-gas, giving a lower silicon yield and a higher energy consumption. An increased pressure in the crater could also cause problems during tapping where you get gassing from the tap hole [5], [6]. A better understanding of what affects the pressure and gas flow in the furnace is thus of importance.

1.2 Objective

The objective of thesis is to investigate how different particle sizes of the raw materials affect the pressure-drop in the charge in furnaces for silicon production. In addition, the effect of different temperatures and different gas velocities will be investigated in regards of the pressure-drop.

The flow of process gasses will be simulated as gas flow through a porous media based on the governing equations of Navier-Stokes describing fluid flow, with Darcy-Forchheimer as a sink-term accounting for the resistance caused by the permeability of the porous media. The simulations will be done using computational fluid dynamics, CFD, in OpenFOAM [7]. The permeability of the zones for the different cases studied will be based on results from previous experimental work done by the author [6], [8].

A part of the objective for this thesis includes understanding of the OpenFOAM software, and developing models for simulating the gas flow and pressure drop of previous results from small-scale experimental work at room temperature. A goal is also to see if these models can be upscaled to simulate the pressure-drop through charge at conditions based on an industrial silicon furnace.

2 Literature Review

2.1 Metallurgical Production of Silicon

Metallurgical grade silicon is produced industrially by reducing silicon dioxide with carbon material such as coal, coke, charcoal, and woodchips. The source of silicon oxide is mainly quartz. The carbothermic reduction happens in submerged arc furnaces, where the raw materials are added from the top. The normal size of the quartz added varies from 10 – 150 mm and the size of the carbon will vary from 1 – 30 mm [1].

As the raw material descends through the arc furnace, several chemical reactions occur with SiC and SiO being produced as intermediate steps before silicon is produced. The SiO gas is one of the main variables deciding the silicon yield [1]. The overall reaction can be written:

$$SiO_2 + 2C = Si + 2CO \tag{2.1}$$

The overall reaction is endothermic and at 2000°C the enthalpy is calculated to be $\Delta H^0_{2000°C}$ = 687 kJ/mol using HSC Chemistry 9 [9].

A silicon furnace typically has a diameter of about 10 m and is filled with charge material from the top. A three-phase current is supplied by three carbon electrodes submerged into the charge. An electric arc of plasma is formed between the electrode and the pool of silicon. Because of ohmic heating, the temperature is approximately 2000°C in the hottest area close to the electrode tip [10]. At this temperature, the silicon dioxide is reduced to molten silicon which is tapped at the bottom through a tubular hole that reaches into the molten silicon from the outside. The tapped silicon is refined by slag treatment or gas purging [1].

2.1.1 Chemical Reactions in the Furnace

As mentioned above the production of silicon includes both SiC and SiO as intermediate products. This makes the process of silicon production more complex than the reaction given in equation (2.1). The silicon process can be described by dividing the furnace into two zones: a high temperature inner zone and a lower temperature outer zone [1].

In the lower temperature zone, the temperature is about 700 - 1300°C. The raw material is added from the top and heated by the rising hot gas. The descending C react with the ascending SiO to form SiC and CO according to equation (2.2). SiO gas will react with CO gas to produce SiO_2 and SiC according to equation (2.3). In addition, SiO gas will self-dissociate to SiO_2 and Si according to equation (2.4) [11].

$$2C_{(s)} + SiO_{(g)} = SiC_{(s)} + CO_{(g)} \quad (2.2)$$

$$3SiO_{(g)} + CO_{(g)} = 2SiO_{2(s,l)} + SiC_{(s)} \quad (2.3)$$

$$2SiO_{(g)} = SiO_{2(s,l)} + Si_{(s)} \quad (2.4)$$

In the hottest inner zone the temperature is around 2000 °C, except from the volumes connected with the arc which have much higher temperatures. In this area the condensed species present are mainly SiO_2 and SiC with some remaining free carbon. At this temperature the free carbon is unstable and will gradually react with SiO or Si to produce SiC. In this area SiO gas is formed through the reactions given in equation (2.5) and (2.6). Si is produced through the reaction between SiO gas and SiC given in equation (2.7) [1].

$$2SiO_{2(s,l)} + SiC_{(s)} = 3SiO_{(g)} + CO_{(g)} \quad (2.5)$$

$$Si_{(l)} + SiO_{2(s,l)} = 2SiO_{(g)} \quad (2.6)$$

$$SiO_{(g)} + SiC_{(s)} = 2Si_{(l)} + CO_{(g)} \quad (2.7)$$

The off-gas from the silicon process consists of SiO gas and CO gas. As silicon is produced in open furnaces with access to air the SiO gas and CO gas reacts with oxygen from the air and burn on top of the charge according to the equations:

$$SiO_{(g)} + \frac{1}{2}O_{2(g)} = SiO_{2(s)} \quad (2.8)$$

$$CO_{(g)} + \frac{1}{2}O_{2(g)} = CO_{2(g)} \quad (2.9)$$

The SiO_2 from the reaction given in equation (2.8) is in the form of microsilica, which is sold as a by-product for use in concrete [1].

A schematic picture of the inner structure of a Si furnace, based on several furnace excavations, is given in Figure 2.1. Main reactions occurring at the different levels of the furnace is given to the right.

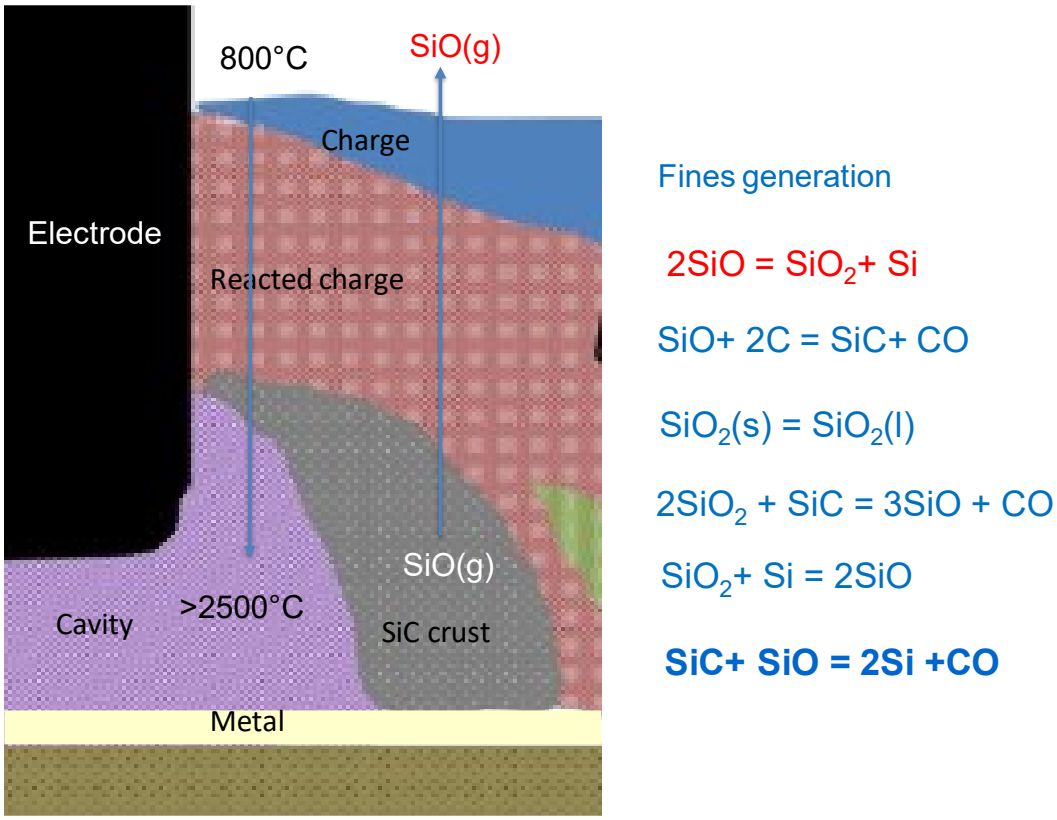

Figure 2.1: Illustration of the inner structure of a Si furnace with reactions taking place. Figure from [12].

2.1.2 Thermodynamics of the System

Calculations of thermodynamic equilibrium give a general understanding of the chemical reactions happening in the furnace, but they do not say anything about the kinetics of the reactions. Equilibrium calculations can show if a reaction is possible at a given temperature and give indications on how the rate can be increased. An estimation of equilibria will therefore give a basic understanding of the system.

In the furnace there will always be one gas phase and several solid or liquid phases in a reaction zone. These reaction zones can be regarded as chemical systems consisting of multiple phases instead of considering different reactions in the zone. The combination of phases at equilibrium will have a certain gas pressure which can be used to estimate the reactions of the reduction process [1]. Gibbs phase rule gives a relation between the number of phases, *Ph*, that can coexist within a system at equilibrium. This relation can be expressed:

$$Ph + F = C + N \tag{2.10}$$

Where F is the number of degrees of freedom or externally controlled variables such as temperature, pressure and composition, C represents the number of components in the system, and N is the number of noncompositional variables [13]. In the furnace the noncompositional parameters are temperature and pressure giving $N = 2$. The components in the system is Si, C and O giving $C = 3$ [1].

A gas phase consisting of mainly SiO and CO is always present in the system. In the Si-O-C system there are four condensed phases in the temperature range of the process: SiO_2, C, SiC, and Si. The thermodynamic variables are temperature, pressure, and composition. The number of condensed phases is thus the variable needed to be fixed to determine the system completely.

For a system with two condensed phases there are six combinations of the possible condensed phases. The combination with Si and C is unstable and will react according to the reaction:

$$Si_{(s,l)} + C_{(s)} = SiC_{(s)} \tag{2.11}$$

If the temperature and the total pressure are fixed, the partial pressure of SiO gas can be shown as a function of temperature. Figure 2.2 Show the SiO partial pressure as a function of temperature at a total pressure of 1 bar for the five combinations of the condensed phases that are of interest for the silicon production process. When the pressure of SiO is higher than the corresponding equilibrium line the reaction is driven to the right. If the pressure of SiO is below the equilibrium line the process will be driven toward the left resulting in consummation of the product species. From Figure 2.2 it can be seen that both a high temperature and a high partial pressure of SiO is necessary to produce silicon through the reaction given in equation (2.7).

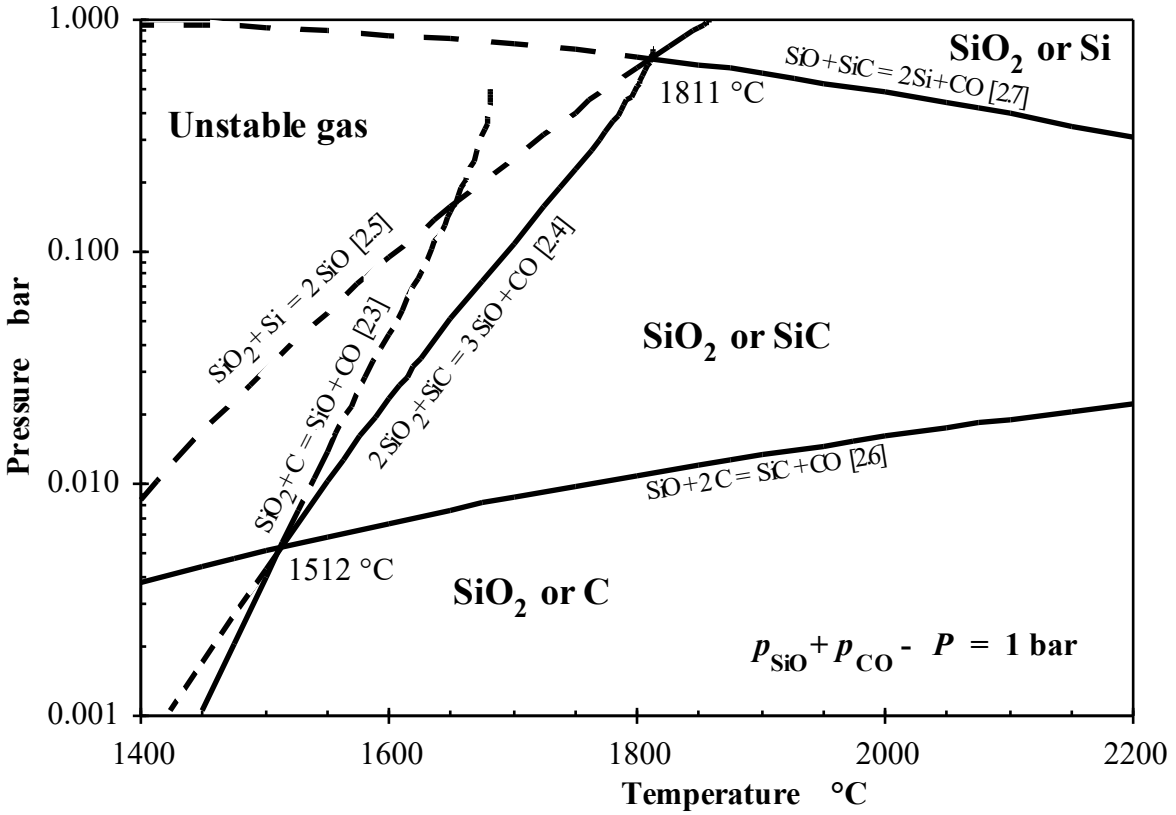

Figure 2.2: Equilibrium diagram for the SiO pressure above the condensed phase combinations C-SiC, SiO_2-C, SiO_2-SiC, SiC-Si, and SiO_2-Si as illustrated by Schei et al [1]. The total pressure is assumed to be 1 bar consisting of only SiO gas and CO gas.

2.1.3 Energy Consumption and Silicon Yield

The carbothermic production of silicon is a highly energy intensive process where a typical silicon furnace has an energy consumption of 11 – 13 MWh per metric ton of silicon produced [1]. The energy consumption is highly dependent on the silicon yield. The silicon yield of the process can be described as the ratio between the silicon in the tapped metal and the silicon added to the furnace as SiO_2 [10].

$$Silicon\ yield = \frac{Silicon\ tapped}{Silicon\ added} \tag{2.12}$$

$$Si\ yield = \frac{Si\ tapped}{Si\ tapped + Si\ in\ SiO\ leaving\ the\ furnace + Si\ in\ accumulated\ SiC} \tag{2.13}$$

To achieve a high silicon yield and a low energy consumption it is important that Si do not leave the furnace through the exhaust system as SiO gas [10]. The reactions at the lower temperature zone in the upper part of the furnace, given in equation (2.2), (2.3), and (2.4), are thus of high importance in retrieving silicon.

$$2C_{(s)} + SiO_{(g)} = SiC_{(s)} + CO_{(g)} \tag{2.2}$$

$$3SiO_{(g)} + CO_{(g)} = 2SiO_{2(s,l)} + SiC_{(s)} \tag{2.3}$$

$$2SiO_{(g)} = SiO_{2(s,l)} + Si_{(s)} \tag{2.4}$$

Kinetic studies have shown that SiO reacts in the gaseous state when combined with either C or SiC, and that the sublimation of SiO gas to Si and SiO_2 in equation (2.4) is not rate determining [14]. The most important reaction is the reaction with carbon given in equation (2.2), as the main part of the SiO gas is recovered by free carbon [1].

The overall reaction of the silicon process can be written:

$$SiO_2 + (1+x)C = xSi + (1-x)SiO + (1+x)CO \tag{2.14}$$

In this equation the silicon yield is represented as *x*. The silicon yield is an important economical factor and is determined by the amount of silicon leaving the furnace as SiO gas. The silicon yield normally lies between 75 – 90 % for the silicon process [15].

2.2 Permeability of Charge Mixtures

In industrial production of silicon there are two ways to charge the furnace: continuous charging or batch charging. Continuous charging is normally done by feeding the furnace around every minute. For this charging method the amount of raw material per feeding is low. This provides a charge surface with an even temperature. In batch charging the furnace is fed with raw material periodically, normally every hour. The amount of raw material per feeding is large [16]. The added quartz normally has a size varying between 10 – 150 mm, while the added carbon has a size varying from 1 – 30 mm [1]. The charge material creates a porous environment with voids between the particles and pore channels through the charge where the process gases can move [17].

The permeability of the charge is dependent on various phenomena including the packing of the raw materials, the formation of fines which clogs the pores, and the formation of a dense

condensate layer of Si, SiO_2, and SiC [6]. A lower permeability causes a higher resistance towards gas flow, which again can cause operational problems.

To achieve a stable and effective furnace operation it is important to have a high and even gas permeability. If the charge mixture is too compact the gas will be hindered from flowing freely through the charge [17]. The gas may be restricted to traveling through channels formed through the charge. The apparent velocity of the gas can be found by dividing the gas flux on the cross-sectional area. As gas traveling through narrow channels has a lower area compared with gas evenly distributed across the entire packed bed, this channel formation will result in a higher gas velocity. A higher gas velocity gives less time for silicon retrieving reactions to occur while the SiO travels through the charge. In addition the channel formation gives less contact area between the SiO gas and free carbon in the charge compared with an evenly distributed gas, which also results in less SiO being recovered from the off gas [6].

2.2.1 Formation of Fines and Clogging

Fines may be defined as material with particle sizes below 5 mm [5]. The disintegration of quartz into fines is an important factor for the furnace operation. A large amount of fines will cause the pores between the larger charge particles to clog and hinder an even gas flow through the charge. Clogging of the furnace can lead to small outbursts of gas or channel formation in the furnace, which lowers the Si-yield as the ascending SiO gas is not retrieved [18]. Figure 2.3 illustrates how the gas flow is affected if the charge contains too much fines.

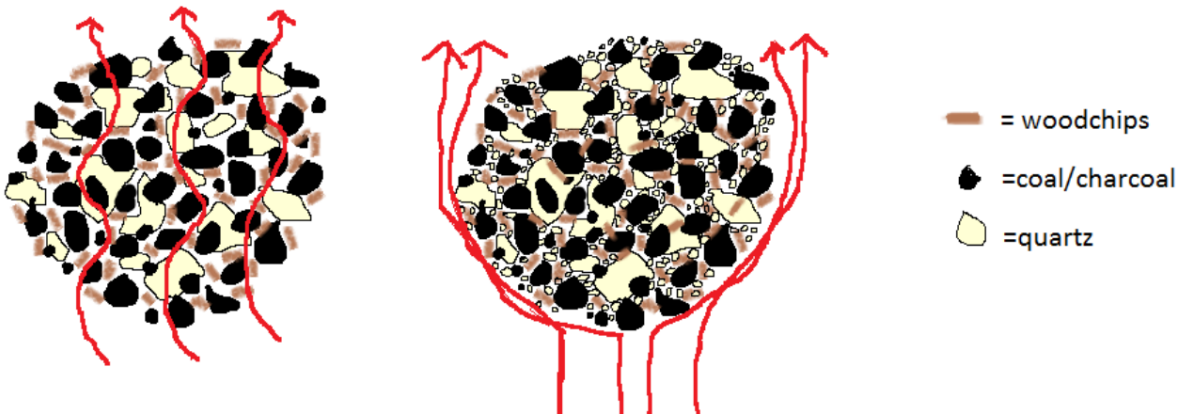

Figure 2.3: Illustration of gas flow in a charge with a low amount of fines (left) and a high amount of fines (right) [18].

For the quartz, fines may form during transport and handling, especially if the mechanical properties of the raw materials are bad. The thermo-mechanical properties of the ore can cause formation of fines within the furnace. With bad thermo-mechanical properties, the extreme heat from the furnace can cause the quartz to disintegrate. Ideally, the quartz should keep its original size as it descends through the furnace until it starts to soften and melt in the lower part of the furnace near the cavity [6], [19].

In limiting the formation of fines, both good mechanical and thermo-mechanical properties are of importance. With a high amount of fines, the permeability of the charge material is lowered. The fines settles in the voids between the bigger particles, clogging the pores [6], [19]. Fines of quartz also gives a higher surface area which results in higher kinetics, producing more SiO gas. For the SiO to react further to produce silicon a high temperature is needed. As the temperature in the higher parts of the furnace is too low for the silicon producing reaction to occur, formation of SiO in these zones are not beneficial. The SiO produced in these parts must be retrieved by the silicon retrieving reactions to not be lost as SiO in the off gas [6], [20].

2.2.2 Condensate Formation

As SiO gas and CO gas produced in the hotter parts of the furnace rise through the charge to the lower temperature zone it is cooled. If the temperature is below the condensation temperature, the condensation of SiO-gas takes place through reaction (2.3) and (2.4). As these are exothermic reactions the amount of silicon to be recovered by condensation is limited. As the reaction proceeds, heat will be released rising the temperature above the condensation point. The layer of formed condensate gives a lower permeability of the charge, causing a resistance to gas flow. This causes a build-up of pressure in the furnace [1], [17].

In the silicon furnace there can be found a stoking crust, a crater crust and a side crust created of accumulated material. The stoking crust is located at the top of tha charge and is where the stoking takes place. The crater crust is located mostly at the center of the furnace and at the cavity walls. The side crust covers the furnace walls internally and can extend up to the charge level. All these crusts contain condensate, but most of the condensate is found at the stoking crust. The stoking crust has a thickens of around 1 m from the charge top [21].

2.3 Different Zones in the Furnace

Excavations of furnaces for silicon production have shown that the furnace consists of different zones with different properties [22], [23]. The creation of these zones is unevitable because of different phenomena such as chemical reactions, uneven heat distribution, softening and melting of quartz, and condensation of process gasses. Excavations have also shown that a cavity is formed low in the furnace close to the electrode tip [24].

2.3.1 Excavations of Si Furnaces

Excavations of different submerged arc furnaces have shown that the furnace consists of multiple zones with different properties. The excavations have shown that a cavity is formed in the lower part of the furnace close to the electrode tip [22], [25], [26]. The size of the cavity increase as the production process proceeds within the furnace [24]. The physical properties of each zone, such as porosity and particle size, define the resistance of the zone toward fluid flow. A reduced permeability of the charge material causes a higher resistance to gas flow of the process gasses which increases the crater pressure [24].

Metallurgical excavations of industrial furnaces are generally carried out as fast as possible followed by rapid reconstruction of the furnaces. The geometry of the zones in the furnace are thus based on visual estimations from the outside of the furnace and samples taken as they are removed from the furnace [25].

An overview of the different zones inside the furnace found at an excavation of a ferrosilicon furnace at Finnfjord is illustrated in Figure 2.4. The raw materials on top of the furnace were loosely packed and no notable transformation was seen in the upper 20 – 30 cm of the furnace charge. Below this top charge, laid an approximately 50 cm horizontal layer of partly reacted raw material, held together with glassy condensates. The crater walls around each of the three electrodes were formed of mainly SiC and metal. These crater walls were dense and extended up through the condensate layer. Several gas channels were observed on the outside of the crater walls, indicating that significant gas transportation takes place outside of the crater. Brown and white condensates were found in a layered structure outside of the gas channels, suggesting the presence of a radial temperature field in the furnace [22].

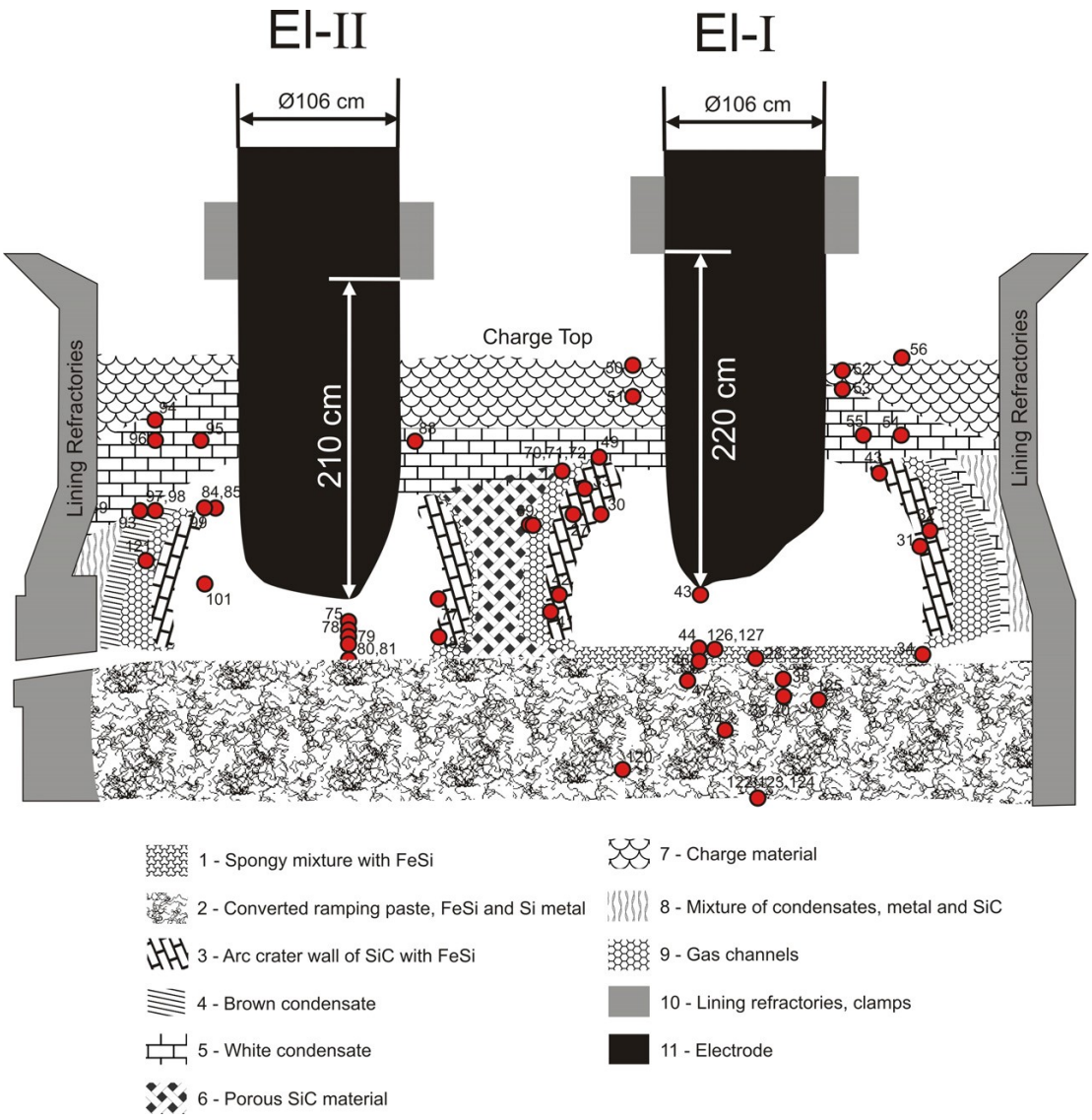

Figure 2.4: Overview of the zones in the furnace around the electrodes from an excavation of a ferrosilicon furnace at Finnfjord [22].

The geometry of the zones within the furnace is however dependant on the operational history. Different furnaces can have several different geometries, sizes, and compositions of the different zones. An illustration of this is visible in Figure 2.5, which shows the zones found from excavations of three different silicon furnaces. The distribution and appearance of the different zones was found to mainly be determined by the furnace operation strategy and not by the materials used [25].

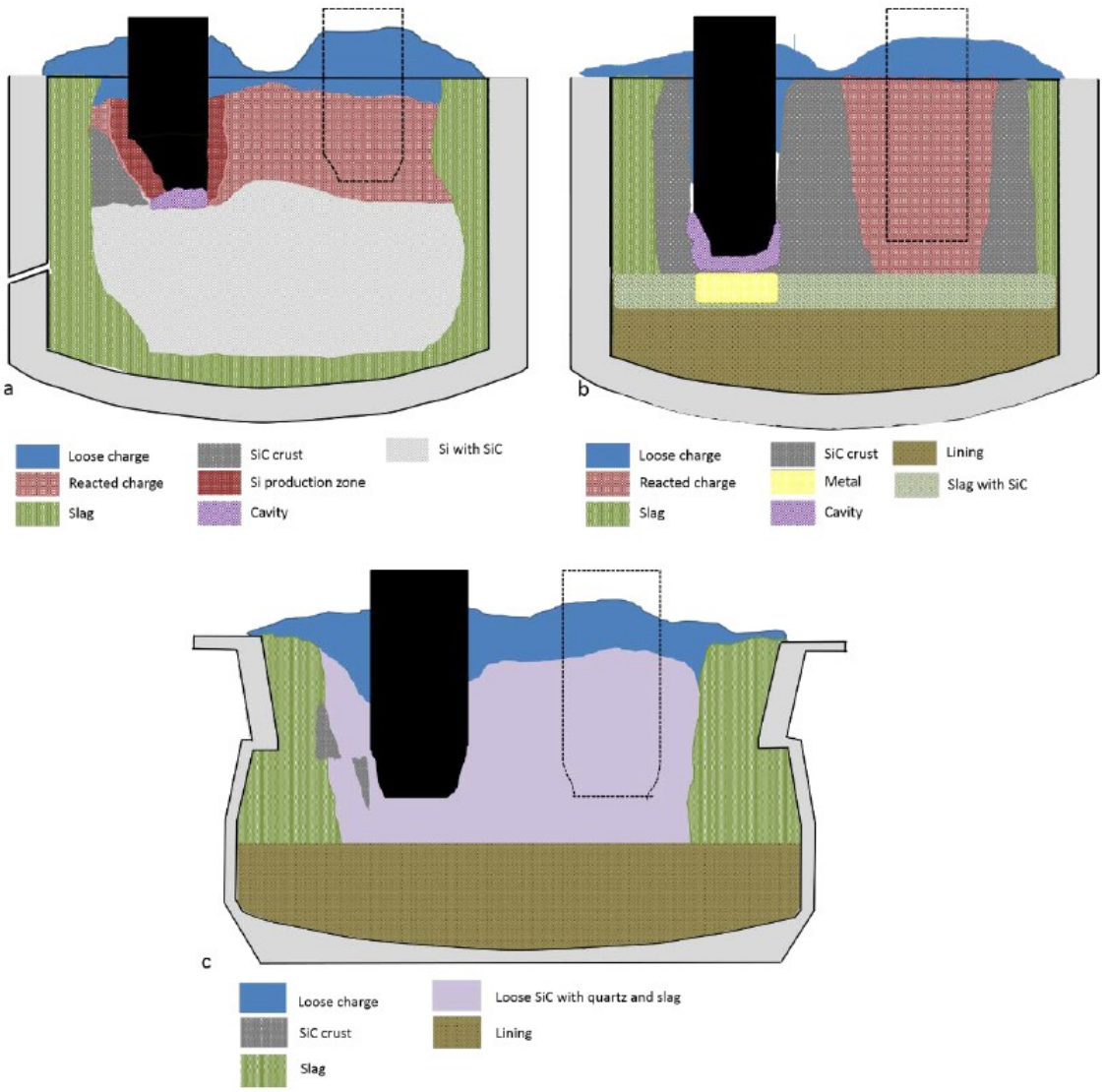

Figure 2.5: Overview of the different zones found from the excavation of three different Si furnaces: a) Wacker furnace no. 1, b) Elkem Thamshavn, c) Wacker furnace no. 4 [25].

2.4 Furnace Crater Pressure

The process gasses in the furnace consists mainly of SiO gas and CO gas. The gas flows from the lower parts of the furnace toward the top by passing through the charge material [24]. In a theoretical silicon process, as an example, with a 20 MW furnace, reactants can be added in a volume of 0.8 litre per second. This gives around 1.3 Nm^3 per second of process gasses. The volume of these gases will be of a even greater order due to the high temperature of the gases. In the lower reaction zone the temperature is about 1800 °C. Simplified it can be stated that 1 litre of reactants is converted to several cubic metres of gasses every second [27].

The permeability of the charge is reduced by different phenomena including the formation of a condensate layer of Si, SiO_2, and SiC, the choice of raw materials, the packing of the raw materials, and formation of fines which clogs the pores in the charge [6], [17]. The production of process gasses in combination with a reduced permeability of the charge results in an increased pressure in the crater zone [24].

Results from industrial measurements have shown that the crater pressure inside the furnace has a dynamic nature [15], [24]. The pressure inside the crater zone is in addition to the permeability of the charge influenced by the rate of reactions happening in this zone, the electrode height, and the applied electrical load. The process of stoking the furnace causes avalanches of charge materials which also have shown to have an effect on the crater pressure [24].

Figure 2.6 shows the crater pressure measured at furnace 2 at Elkem Thamshavn [15]. In this figure the dynamic nature of the pressure drop can be seen. It can also be seen a correlation between crater pressure and furnace load. This correlation can be explained by the fact that the furnace load controls the reaction rate of the reactions occurring in the inner parts of the furnace. Researchers from Icelandic Alloys has also measured the crater pressure and found it to vary between 2 and 10 kPa [26]. This corresponds well with the measurements from Elkem Thamshavn.

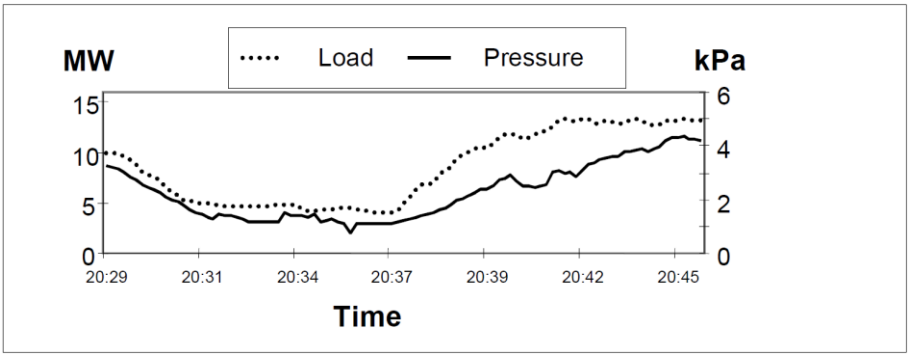

Figure 2.6: Crater pressure and electrode load measured at furnace 2 at Elkem Thamshavn [15]

At Elkem Thamshavn, the crater pressure has also been measured over a longer time interval. The crater pressure was measured at electrode 2 and electrode 3 and was compared with dust in the off-gas, temperature and stoking. During the stoking process, the pressure increased under the electrodes. This is because stoking clogs the void around the electrodes and reduces the permeability in the charge. This can give a more effective condensation of SiO gas which gives a higher silicon yield. The pressure decreases again between stoking. There is no visible correlation between the pressures measured at the different electrodes. This indicates that the craters around the different electrodes are relatively independent of each other [28].

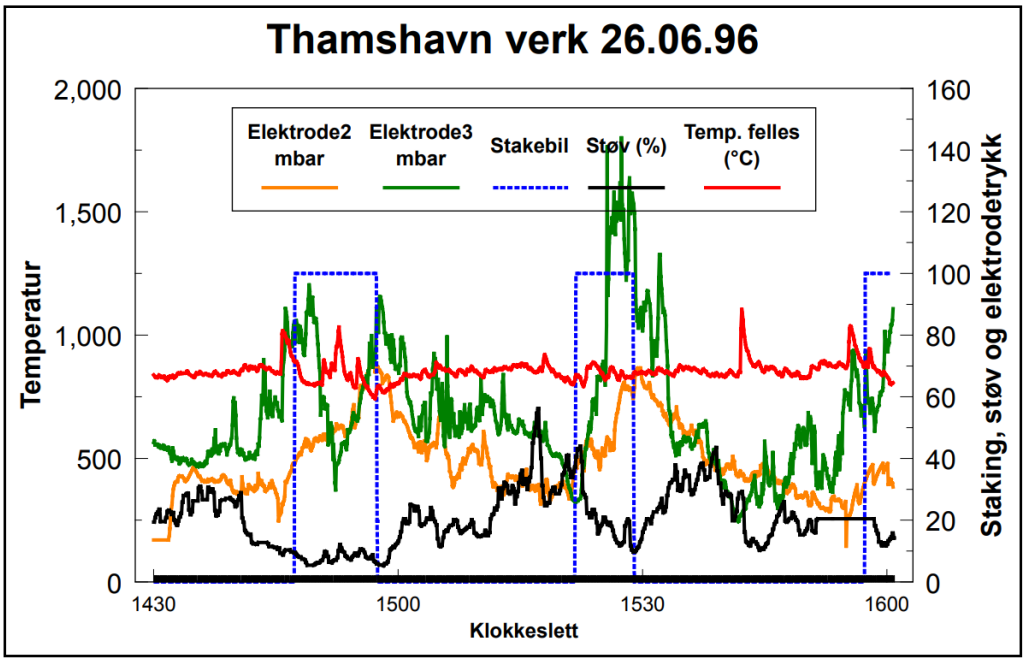

Figure 2.7: Measurements of pressure at different electrodes in the furnace compared with stoking (blue line), % dust (black line) and temperature (red line) under continuous feeding of raw materials [28].

The crater pressure in the furnace has been modelled using computational fluid dynamics, CFD, by Kadkhodabeigi [29]. The modelled pressure patterns inside the furnace are shown in Figure 2.8. The pressure is higher in the crater zone compared with other regions of the furnace. From the calculations the pressure in the lower part of the furnace was also found to decrease with increasing distance from the furnace centre.

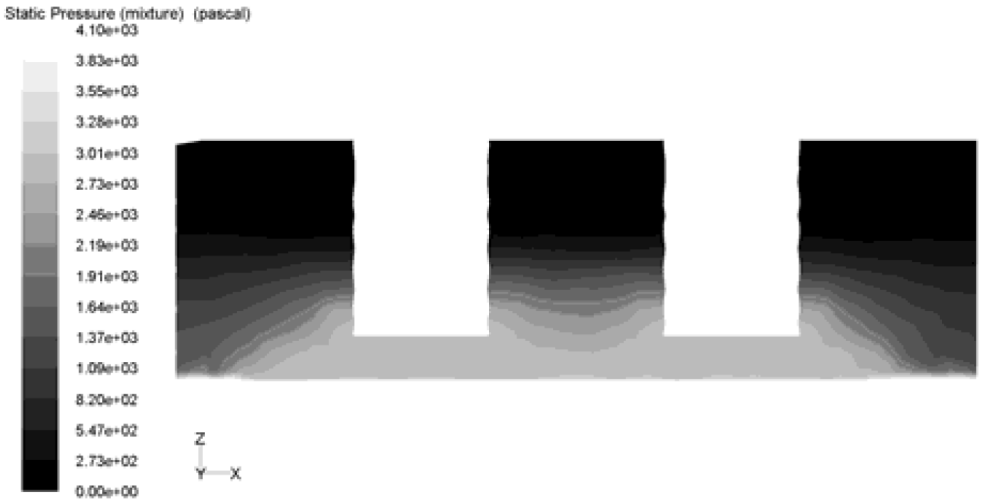

Figure 2.8: 2D contours of simulated pressure pattern around two electrodes above the melt in the silicon furnace [29].

The pressure in the furnace has also been modelled and simulated by Edfeldt based on experimentally measured pressure through different charge mixtures [17]. Figure 2.9 shows the simulated pressure from gas flow in a 40 MW silicon furnace plotted as a function of the particle sphericity. The sphericity of the particles of the charge for silicon production is in the range of 0.75 – 1. The results found that particles at 4.76 mm and above resulted in a pressure drop lower than the 30 mbar line, representing the pressure seen during stable operation of the furnace. The higher peaks from pressure measurements of industrial furnaces were thus found to most likely be a result of other factors than the particle sizes and packing of the raw material. These peaks are more likely due to condensation of SiO clogging the charge [17].

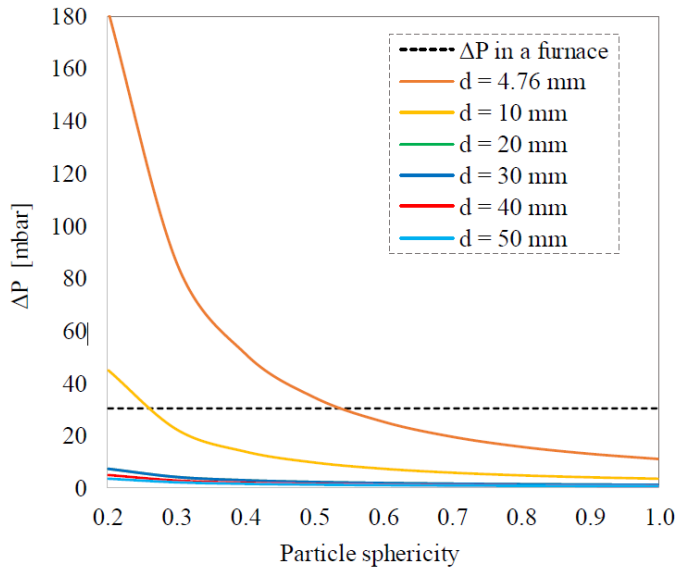

Figure 2.9: Simulated pressure drop from gas flow in a 40 MW silicon furnace for different particle sizes plotted as a function of particle sphericity. The dotted black line show a basis pressure in an industrial furnace [17].

2.5 Gas Flow Through Porous Media

The behaviour of gas flowing through a porous media can be described using fluid dynamics, which is the study of fluids in motion. In fluid dynamics, all matter consists of only two states: fluid and solid. In the case of gas flow through porous media the gas is regarded a fluid moving through a porous solid material which causes resistance to the fluid flow [30].

2.5.1 Pressure-Drop in Packed Beds

In the silicon furnace, the charge material above the crater wall can be regarded as a packed bed. A packed bed is made up of particles in a container through which a fluid flows. This fluid can be both a gas or a liquid. The particles lay at rest on top of each other, and ideally there is no relative motion between the particles. At the bottom and at the walls of the container, the packed bed is considered completely at rest. The fluid is distributed uniformly across the cross-sectional area of the packed bed. The volumetric flux is constant and is referred to as the fluid velocity in reference to the *"empty bed"*. The volumetric flux can be written:

$$V = \frac{\dot{V}_f}{A_0} \tag{2.15}$$

where $\dot{V}_f$ is the volumetric flow and A_0 is the area of the bed [8], [31]. The gas flow through a packed bed has been studied widely and was mathematically described in 1952 by Ergun. The pressure drop across a packed bed can be calculated using Ergun's formula [32]:

$$\frac{\Delta P}{L} = A\frac{(1-\varepsilon)^2}{\varepsilon^3}\frac{\dot{\mu}}{\varphi^2 d_p^2}V + B\frac{1-\varepsilon}{\varepsilon^3}\frac{\rho}{\varphi d_p}V^2 \tag{2.16}$$

ΔP is the pressure drop, L is the hight of the packed bed, V is the volumetric flux corresponding to the fluid velocity in reference to an empty bed, ε is the void fraction of the packed bed, ρ is the density of the fluid, μ is the viscosity of the fluid, d_p is the equivalent spherical diameter of the particles and φ is the particle sphericity [6], [32].

In equation (2.16) the first term with the velocity in the first order is the laminar component. This is the term dominating at lower velocities, representing the viscous losses proportional to the fluid velocity. The second term, with velocity in the second order, is the turbulent component. This term dominates at higher velocities and represents internal losses which are proportional to the velocity squared. The constants A and B were determined by Euler to be 150 and 1.75 respectively. These are constants that are applicable for systems where the particles have sphericity close to unity. For systems where the particles are irregularly shaped, this model systematically under predicts the pressure drop [5], [6], [32].

Another model describing the pressure drop across a packed bed is the Darcy-Forchheimer equation [33]:

$$\Delta P = \frac{\mu L}{k_1}\dot{V}_f + \frac{\rho L}{k_2}\dot{V}_f{}^2 \tag{2.17}$$

In this relation the material parameters in Erguns equation is described by the constants k_1 and k_2. These material parameters are often unknown, and k_1 and k_2 can be found by fitting experimental data.

When simulating the flow through a porous media the viscous losses and dissipation losses is described by the Darcy-Forchheimer coefficients: *D* and *F*. The Darcy-Forchheimer equation is rewritten as:

$$\frac{\Delta P}{\Delta L} = \mu \boldsymbol{D} V + \frac{1}{2}\rho \boldsymbol{F} V^2 \tag{2.18}$$

D and F can be found from k_1 and k_2 by the relations:

$$D = \frac{1}{k_1} \tag{2.19}$$

$$F = \frac{2}{k_2} \tag{2.20}$$

Both the Ergun equation given in (2.16) and the Darcy-Forchheimer equation given in (2.17) and (2.18) is defined in one dimension, and it is assumed incompressible flow, meaning that the density of the fluid is constant. In one dimension this also results in the flow being restricted to constant velocity.

2.5.2 General Description of Fluid Flow

The governing equations for describing fluid flow is the continuity equation and Newtons 2. law. The continuity equation can be written:

$$\frac{d\rho}{dt} + \nabla(\rho \boldsymbol{u}) = 0 \tag{2.21}$$

The continuity equation states that there is no global change in mass and thus mass is conserved. The first term, $\frac{d\rho}{dt}$, represents the accumulation of mass per volume and the second term, $\nabla(\rho \boldsymbol{u})$, represents the flux of mass per volume. This is true for all control volumes [30].

Newtons second law for fluid elements can be written:

$$\frac{d}{dt}(\rho \boldsymbol{u}) + \nabla(\rho \boldsymbol{u}\boldsymbol{u}) = -\nabla p + \nabla \cdot \tau + \rho \boldsymbol{F} \tag{2.22}$$

Newtons second law states that mass times acceleration, or the change in momentum, equals the sum of forces. The left-hand side represents the change in momentum where the first term, $\frac{d}{dt}(\rho \boldsymbol{u})$, is the acceleration of mass per volume and the second term, $\nabla(\rho \boldsymbol{u}\boldsymbol{u})$, is the net flux of momentum per volume. The right-hand side of the equation represents the sum of forces. The two first terms on the right-hand side represents the internal forces, where ∇p is the pressure forces where a gradient in pressure causes a fluid to move, and $\nabla \cdot \tau$ is the viscous forces which causes resistance to fluid motion. The last term on the right-hand side represents all external forces. Usually this would be the gravitational force [34].

By assuming incompressible fluid, meaning that the density is constant, the continuity equation can be simplified to:

$$\nabla \boldsymbol{u} = 0 \tag{2.23}$$

By also assuming Newtonian fluid and constant viscosity, μ, the term with the viscous forces can be rewritten:

$$\nabla \tau = \mu \nabla^2 \boldsymbol{u} \tag{2.24}$$

With these assumptions the Navier-Stokes equation for incompressible fluids can be written:

$$\nabla \boldsymbol{u} = 0 \tag{2.23}$$

$$\rho \frac{d\boldsymbol{u}}{dt} = -\nabla \boldsymbol{p} + \mu \nabla^2 \boldsymbol{u} + \rho \boldsymbol{F} \tag{2.25}$$

The Navier-Stokes equations are second order nonlinear partial differential equations describing fluid flow. These equations have a limited number of known analytical solutions, but they are used in computational fluid dynamics, CFD, to find approximate results to a wide variety of two- and three-dimensional viscous flows [30].

When modelling flow through a porous media using OpenFOAM [7] the Darcy-Forchheimer acts as a sink term, S_m, in the Navier-Stokes equations.

$$\frac{d}{dt}(\rho \boldsymbol{u}) + \nabla(\rho \boldsymbol{u}\boldsymbol{u}) = -\nabla p + \nabla \cdot \tau + S_m \tag{2.26}$$

The equation for the sink term can be written:

$$S_m = -\left(\mu D + \frac{1}{2}\rho |\boldsymbol{u}| F\right)\boldsymbol{u} \tag{2.27}$$

Where D and F are the Darcy-Forchheimer coefficients as described in section 2.5.1 [35], [36].

2.6 Measurements of Pressure Through Charge

In previous work done by the author the pressure drop was measured through different charge mixtures experimentally at room temperature. The packed beds contained either quartz, coal and woodchips or quartz and coal without woodchips, where the size fractions of quartz and coal were varied.

Both the quartz and coal were sieved into four different size fractions, with fractions as given in Table 2.1.

Table 2.1: Size fractions used for quartz and coal [6].

Material	*Size fraction* [*mm*]
Quartz	0.00 – 0.25
	0.25 – 2.00
	2.00 – 4.75
	4.75 – 10.00
Coal	0.00 – 2.00
	2.00 – 3.35
	3.35 – 5.00
	>5.00

The size fractions used were based on sieve curves to get the optimal utilization of the delivered material.

The apparatus used for the experiments was a custom built rig which was developed as a part of a project work in 2018 by Hanne Edfeldt [5]. The test apparatus is schematically illustrated in Figure 2.10. The pressure drop apparatus consist of an acrylic cylinder with a height of 1 m and an inner diameter of 185 mm. Three differential pressure sensors are mounted along the wall of the cylinder with a 30 cm spacing with the first sensor at the base of the cylinder. Compressed air enters the cylinder at the base and passes through a porous disc which acts both as a separator between the charge and the gas delivery system and distributer plate which ensures an evenly distributed gas flow through the charge. During the experiments the air has a successively increasing velocity. The gas flow entering the cylinder is regulated by a

Bürkert 8802 pneumatic controlled process control valve and two Bronkhorst mass flow controllers [5], [6].

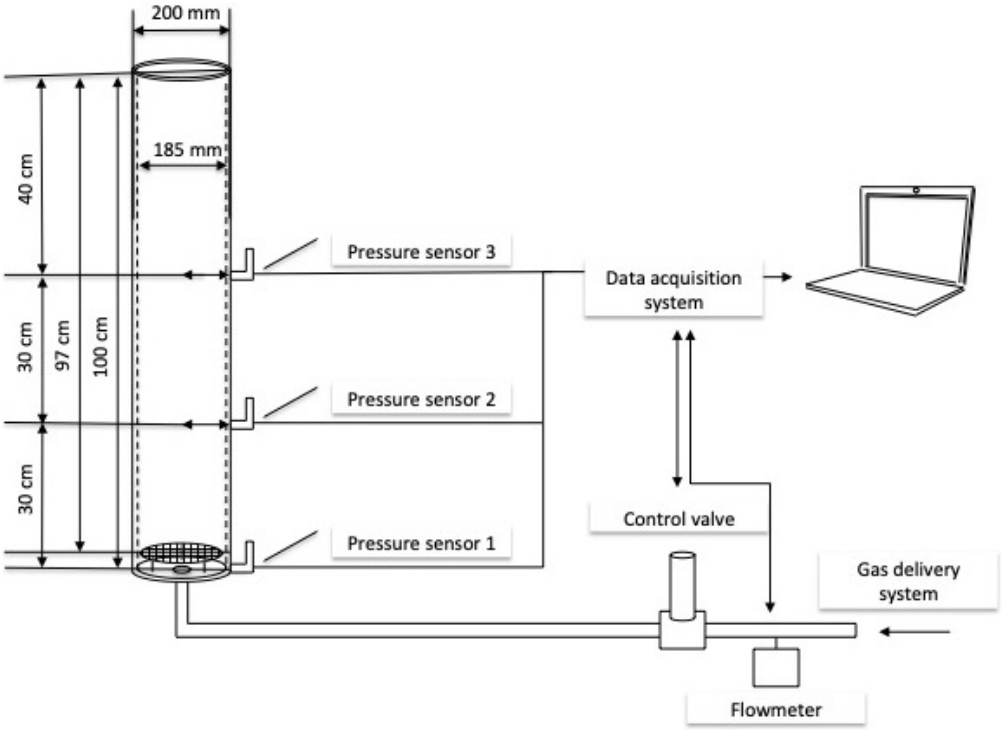

Figure 2.10: A schematic representation of the pressure drop apparatus. Illustration from [5].

The charge mixture for the packed beds were prepared with either coal, quartz, and woodchips or only coal ad quartz. For the experiments with coal, quartz, and woodchips there were used quartz in the size fraction 2.00 – 4.75 mm, and unsieved coal. There was also done an experiment without woodchips to study the effect adding woodchips had on the measured pressure [8]. For the experiments with quartz and coal, all combinations of the different size fractions were used [6]. The raw materials were mixed to a homogeneous mixture before it was added to the cylinder for the pressure tests. For the experiments the cylinder was only filled 70 % to avoid material being ejected out of the cylinder by the gas flow. For all experiments there were done two runs. Run 2 was done directly after Run 1 to study the effect of segregation.

An average pressure drop was calculated for each gas velocity from the measured pressure, and a regression line was found based on these values. Data from the pressure sensor at the lowest position was used for the regression analysis. The regression model was fitted based on the Darcy-Forchheimer equation (2.17) by means of the least squares' method.

Estimated regression lines for the experiments with packed beds with and without woodchips with quartz in the size fraction 2.00 – 4.75 mm and unsieved coal is given in Figure 2.11. The packed beds containing woodchips showed a lower estimated pressure compared with the packed beds without woodchips. The pieces of woodchips used for the experiments were relatively large compared with the coal and quartz which could have caused a higher void fraction and thus a higher permeability explaining the difference in pressure. The packed beds containing woodchips also showed a larger difference between Run 1 and Run 2, indicating that the packed beds containing woodchips has a higher degree of segregation and channel formation.

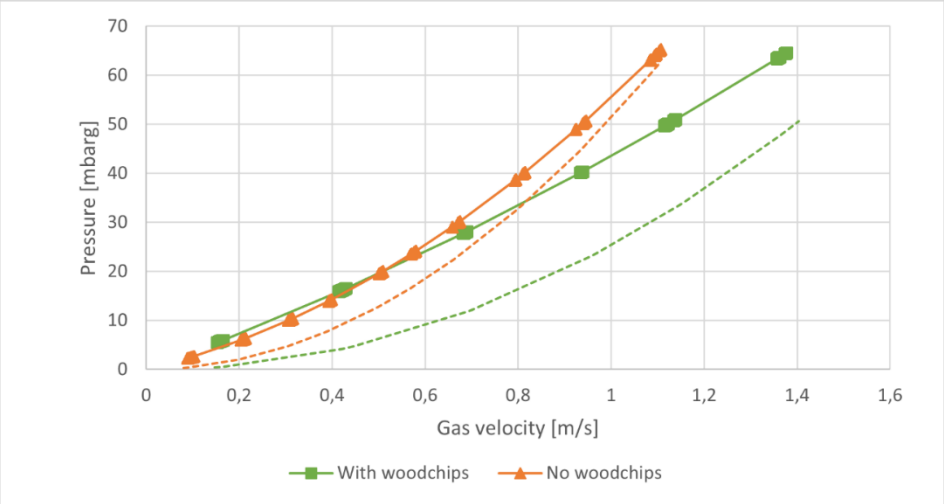

Figure 2.11: Estimated pressure for the packed beds with a homogeneous mixture of coal and quartz with and without woodchips. The regression is estimated from data from the pressure sensor at the lowest position. The continuous line represents Run 1 and the truncated line represents Run 2 [8].

The Darcy-Forchheimer coefficients for the packed bed containing woodchips was not calculated as a part of previous work. The regression analysis was redone on the original data set in the same manner as the results from the packed beds containing only coal and quartz to get comparable results. The new estimated regression line is given in Figure 2.12 with a 95 % confidence interval

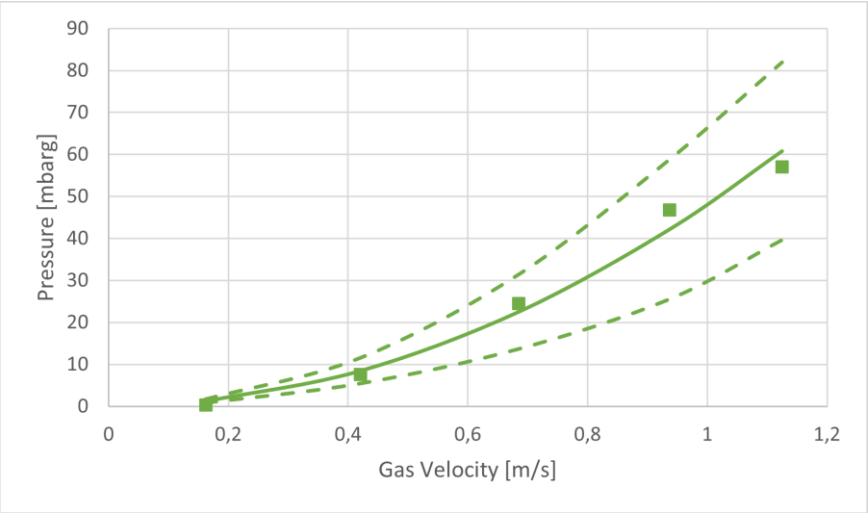

Figure 2.12: Estimated regression line for the pressure drop as a function of velocity for the packed bed containing woodchips, unsieved coal, and quartz at 2.00 – 4.75 mm. The indicators show the average pressure values at a given velocity and the dotted lines show a 95 % confidence interval for the regression line.

Estimated regression lines for all the different size fractions of coal and quartz in the size fractions 0.25 – 2.00 mm, 2.00 – 4.75 mm, and 4.75 – 10 mm are given in Figure 2.13, Figure 2.14, and Figure 2.15 respectively. Coal in the size fraction 0.00 – 2.00 mm is only shown in one of the plots. This is because all but one of the experiments with coal in this size fraction showed significant movement of the charge and could not be considered packed beds. This is also the case for all experiments with quartz in the smallest size fraction 0.00 – 0.25 mm.

The estimated pressure drop was found to be higher for lower particle sizes for both coal and quartz. The estimated pressure was significantly higher when the particle size of quartz was below 2.00 mm. For coal however, all experiments except one with coal in the size fraction 0.00 – 2.00 mm cased the charge to turn into a fluidised bed and the coal was easily carried to the top of the packed bed or into the exhaust system. Smaller particles of coal thus caused a significant segregation of the charge material. The results from this study indicated that the size fraction of quartz had a greater effect on the pressure-drop compared with the size fraction of coal.

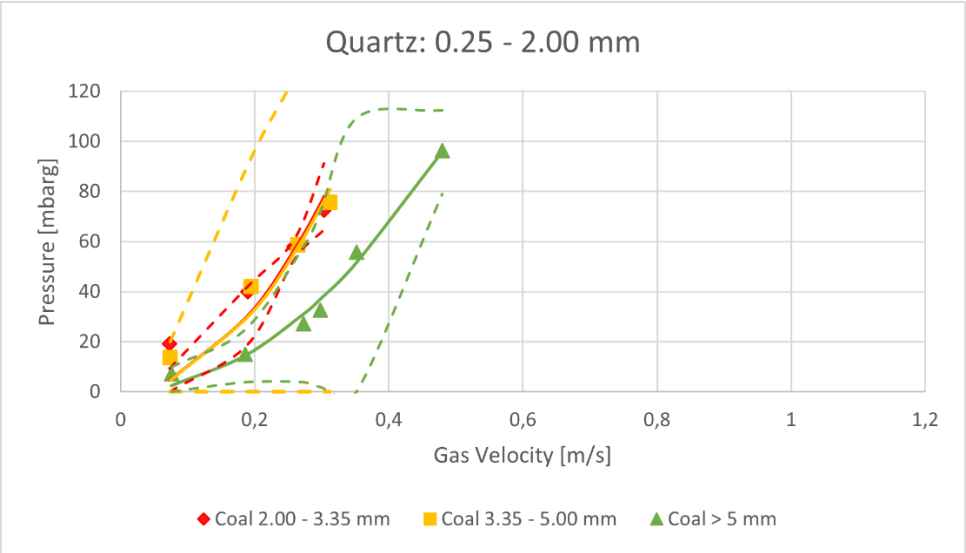

Figure 2.13: Estimated regression lines for the pressure drop as a function of velocity for all size fractions of coal with quartz at the size fraction 0.25 – 2.00 mm. The indicators show the average pressure values at a given velocity and the dotted lines show a 95 % confidence interval for the regression line of the corresponding color [6].

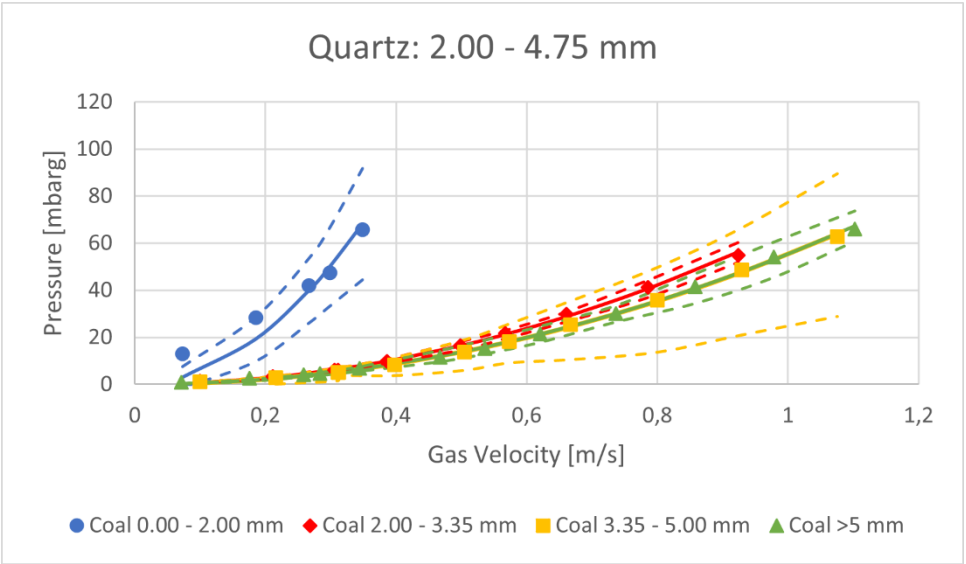

Figure 2.14: Estimated regression lines for the pressure drop as a function of velocity for all size fractions of coal with quartz at the size fraction 2.00 – 4.75 mm. The indicators show the average pressure values at a given velocity and the dotted lines show a 95 % confidence interval for the regression line of the corresponding color [6].

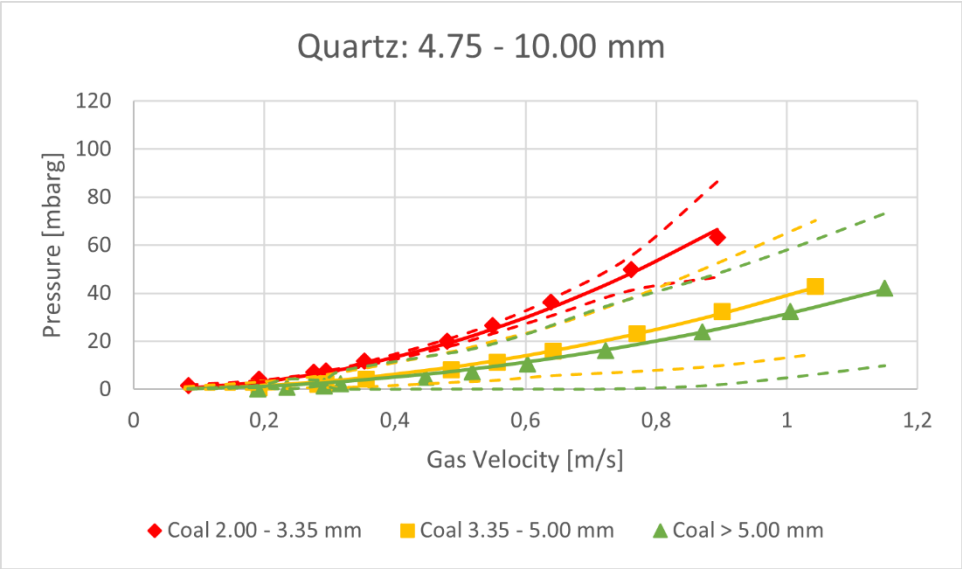

Figure 2.15: Estimated regression lines for the pressure drop as a function of velocity for all size fractions of coal with quartz at the size fraction 4.75 – 10.00 mm. The indicators show the average pressure values at a given velocity and the dotted lines show a 95 % confidence interval for the regression line of the corresponding color [6].

The values for *D* and *F* were calculated as a part of the linear regression analysis and is given in Table 2.2. The number of decimals is not applicable for the physical system studied, but are numerical values obtained when minimizing the error of the regression line.

Table 2.2: Calculated values for the Darcy-Forchheimer coefficients D and F [6], [8].

Size fraction quartz [mm]	***Size fraction coal [mm]***	***D* [-]**	***F* [m^{-1}]**
0.25 – 2.00	*2.00 – 3.35*	*160.593233*	*204331.16*
	3.35 – 5.00	*160.593313*	*200406.09*
	5.00 <	*160.593506*	*100508.313*
2.00 – 4.75	*0.00 – 2.00*	*135.36348*	*135236.284*
	2.00 – 3.35	*135.363751*	*15859.6506*
	3.35 – 5.00	*135.363801*	*13339.7405*
	5.00 <	*135.364059*	*13360.6556*
4.75 – 10.00	*2.00 – 3.35*	*135.364864*	*20124.6453*
	3.35 – 5.00	*135.364685*	*9403.48588*
	5.00 <	*135.364675*	*7577.59994*
Coal, quartz, and woodchips		*100.00138*	*11593.1107*

2.7 Simulating Fluid Flow Using CFD in OpenFOAM

Computational fluid dynamics, CFD, is the study of systems involving fluid flow, heat transfer and associated phenomena including chemical reactions by means of computer-based simulations [37]. Any fluid motion is governed by the three fundamental principles: conservation of mass, conservation of energy and Newtons second law stating that the force is equal to mass times acceleration. These fundamental principles can be expressed as mathematical equations. In computational fluid dynamics the governing equations are solved numerically to obtain a description of the flow field of interest [34].

OpenFOAM, Open source Field Operation And Manipulation, is a free, open source CFD software [38]. The program is the leading open source software for computational fluid dynamics, developed primarily by OpenCFD Ltd since 2004 [39]. OpenFOAM is written in the programming language C++ and contains several numerical solvers for CFD [38].

2.7.1 Solvers for Flow Through Porous Media

Two solvers for simulating flow through porous media is porousSimpleFoam [40] and rhoPorousSimpleFoam [41]. The porousSimpleFoam solver is a steady-state solver for incompressible, turbulent flow through porous media. The solver solves Navier-Stokes equation in the incompressible form given in (2.23) and (2.25) with Darcy-Forchheimer added as a sink term [35]. This solver is located in the following directory in OpenFOAM:

```
$FOAM_SOLVERS/incompressible/simpleFoam/porousSimpleFoam
```

The whole directory includes the files given in Figure 2.16.

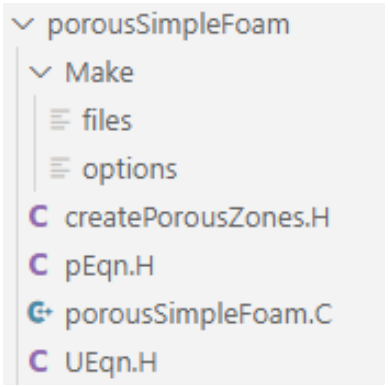

Figure 2.16: Files in the porousSimpleFoam solver.

The make folder is needed in C++ to compile the application. The file porousSimpleFoam.C is the main file in the solver. The files ending with .H are header files. In these files classes being used in the main file are being created. The header files are included in the main file using:

```
# include "filename.H"
```

Where *filename* is the actual name of the .H file.

In the createPorousZones.H, the porous zones are created. In the UEqn.H the momentum equation is constructed and the resistance from Darcy-Forchheimer is added as a sink term. In the pEqun.H the pressure equation is added [42].

The rhoPorousSimpleFoam solver is a steady-state solver for turbulent flow of compressible fluids through porous media. The solver solves the general Navier-Stokes equations for compressible fluids given in (2.21) and (2.22) with Darcy-Forchheimer as a sink term. This solver is located in the following directory in OpenFOAM:

```
$FOAM_SOLVERS/compressible/rhoSimpleFoam/rhoPorousSimpleFoam
```

The whole directory has identical filenames as the files in porousSimpleFoam with the exception of the main file which here is rhoPorousSimpleFoam.C.

2.7.2 File Structure in OpenFOAM Cases

The structure of a basic directory for a OpenFOAM case, that contains the minimum set of files required to run an application is given in Figure 2.17.

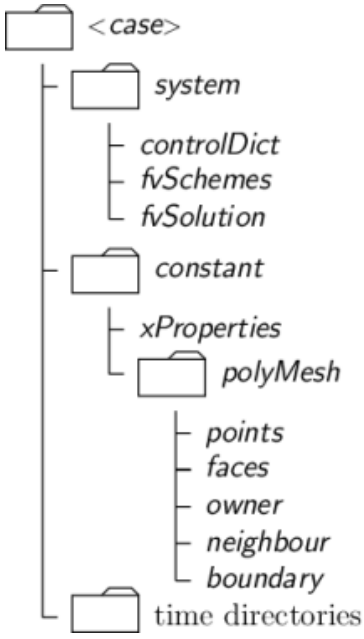

Figure 2.17 Case directory structure in OpenFOAM. Picture from [43].

The *system* directory includes files for setting parameters associated with the solution procedure itself. This directory must at least include the *controlDict*, the *fvSchemes*, and the *fvSolution* files. The *controlDict* is where the run control parameters are set. This includes start- and end-time, time steps and parameters for data output. In *fvSchemes* the discretization schemes used in the solution is selected. In *fvSolution* the equation solvers, tolerances and other algorithm controls are set for the run.

The *constants* directory contains a full description of the mesh of the case in the subdirectory *polyMesh*. In addition, this directory includes files specifying physical properties for the case. This could include for instance transport properties and porosity properties.

The *time* directories contain individual data files for particular fields, for instance velocity and pressure. The data in these files could be either initial values and boundary conditions specified by the user, or results from the simulation written to file by OpenFOAM. As the simulations usually are started at time $t = 0$, the initial conditions are normally stored in a directory named 0 [43].

The structure of the directory of an OpenFOAM case with the required files to run an application with the *porousSimpleFoam* solver is shown in Figure 2.18.

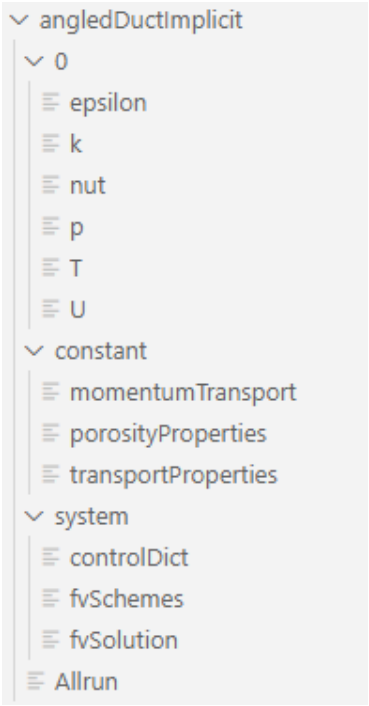

Figure 2.18: Case structure of the tutorial case for the porousSimpleFoam solver.

The 0 folder includes six files. The three first files, *epsilon, k,* and *nut*, are initial turbulence properties where *epsilon* is the turbulent kinetic energy dissipation rate, *k* is the turbulent kinetic energy, and *nut* is the turbulent kinematic viscosity. The files *p, T, and U* includes initial conditions for pressure, temperature, and velocity.

In the constant colder there are three files. In *momentumTransport* the model for momentum transport is set. In *porosityProperties* the resistance to flow is set by the Darcy-Forchheimer coefficients. In *transportProperties* the viscosity is set. The density of the fluid is not of importance as this is an incompressible solver. Because of this, the kinematic viscosity of the fluid is used [44].

The structure of the directory of an OpenFOAM case with the required files to run an application with the *rhoPorousSimpleFoam* solver is shown in Figure 2.19.

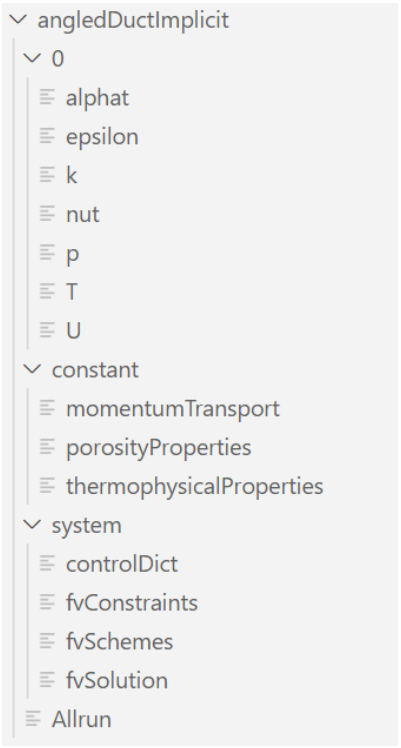

Figure 2.19: Case structure for the tutorial case for the rhoPorousSimpleFoam solver.

The 0 folder is similar to the 0 folder in the incompressible case, but with the addition of the file *alphat*. This file defines the turbulent thermal diffusivity. In the folder with constants, the *transportProperties* file from the incompressible solver is replaced by the file *thermophysicalProperties*. In this file both type of fluid, specie properties, thermodynamic properties and transport properties are defined.

3 Methodology

The pressure-drop caused by process gasses flowing through the charge in a silicon furnace is studied. Experimental measurements of pressure-drop through industrial charge mixtures from a previous study is presented in section 2.6. These measurements are used as a basis for the permeability of different charge mixtures. In this thesis the effect of particle size, temperature, and gas velocity will be studied in regards of the pressure.

The study is based on a theoretical industrial silicon furnace of 45 MW with three 1700 mm electrodes. The gas flow will be simulated using CFD, solving the Navier-Stokes equations with Darcy-Forchheimer added as a sink term. The simulations will be done using OpenFOAM [7]. Firstly, the small-scale cold experiments from a previous study will be simulated. These experiments have both known geometry and boundary conditions. The results from these simulations will be used to validate the models. The simulations will then be upscaled to represent industrial conditions.

The simulations for this thesis are however not meant to be used as simulations of gas flow through an actual furnace but is a parametric study investigating the effect different parameters can have in relation to an industrial furnace.

3.1 Choice of Cases and Parameters

Three different cases will be studied in this thesis. The different cases correspond to different packed beds with different particle sizes and permeabilities based on experimental measurements. Case 1 corresponds to charge material with quartz at 0.25 – 2.00 mm and coal at 2.00 – 3.35 mm, Case 2 corresponds to charge material with quartz at 2.00 – 4.75 mm and coal at 5.00 mm to approximately 10 mm, which was the approximate upper size limit for the delivered coal, and Case 3 corresponds to charge material with quartz at 2.00 – 4.75 mm, coal below 10 mm, and woodchips at 2 – 3 cm. The three cases are given in Table 3.1. The different cases will be studied at three different temperatures chosen for the study: 1750 °C, 1400 °C, and 700 °C. For Case 2 simulations are run at 1400 °C with three different velocities: 1.10 m/s, 0.91 m/s, and 0.53 m/s.

The three different cases were chosen based on previous experimental measurements. Results from experimental work showed that packed beds with larger particle sizes had a significantly

lower effect on the build-up of pressure compared with packed beds with smaller particles sizes. Because of this only charge material with lower particle sizes is studied in this thesis. The experimental work also showed that there was a significant difference between particle sizes above and below 2.00 mm, especially for quartz. The different experiments above 2.00 mm did however not show a significant difference. Because of this there will in this project be investigated pressure drops from three different charge mixtures: two charge mixtures with only coal and quartz where one has quartz above 2.00 mm, and the other has quartz below 2.00 mm, and a third charge mixture containing quartz, coal, and woodchips. The experiments have been chosen as these showed a high difference in expected pressure and a relatively low variability.

The temperatures were chosen based on temperatures of the gas in the industrial silicon furnace [45]. The gas velocities was calculated based on these velocities and the assumption of a 45 MW furnace with 1700 mm electrodes. Calculations of gas velocities are given in section 3.3. The different gas velocities for Case 2 at 1400 °C were chosen to match the velocities at 700 °C and 1750 °C. This is to study the effect of velocity and temperature separated.

Table 3.1: Description of the three cases studied with material sizes and the Darcy-Forchheimer coefficients D and F.

Case	***Material***		***D* [-]**	***F* [m^{-1}]**
Case 1	*Quartz:*	*0.25 – 2.00 mm*	*160.593233*	*204331.16*
	Coal:	*2.00 – 3.35 mm*		
Case 2	*Quartz:*	*2.00 – 4.75 mm*	*135.364059*	*13360.65*
	Coal:	*5.00 mm - 10 mm*[(1)]		
Case 3	*Quartz:*	*2.00 – 4.75 mm*	*100.00138*	*11593.11*
	Coal:	*< 10 mm*[(2)]		
	Woodchips:	*2 – 5 cm*[(3)]		

1. The upper limit of the delivered coal was approximately 10 mm.
2. For Case 3 the coal was unsieved
3. The delivered woodchips varied in both size and shape. The size range is an approximation from manual measurements.

3.2 Geometry for Simulations of Gas Flow in an Industrial Furnace

The geometry for the upscaled simulations is based on a 45 MW furnace with electrodes of diameter 1700 mm. As the active zone is closest to the electrodes it is assumed that 70 % of the produced gas rises through the charge within the area 0.5 meter from the electrode. The area being studied is 0.5 m from the wall of the electrode in width and a height of 1.5 m [45].

The area from the furnace that the geometry of the simulation is based on is illustrated in Figure 3.1.

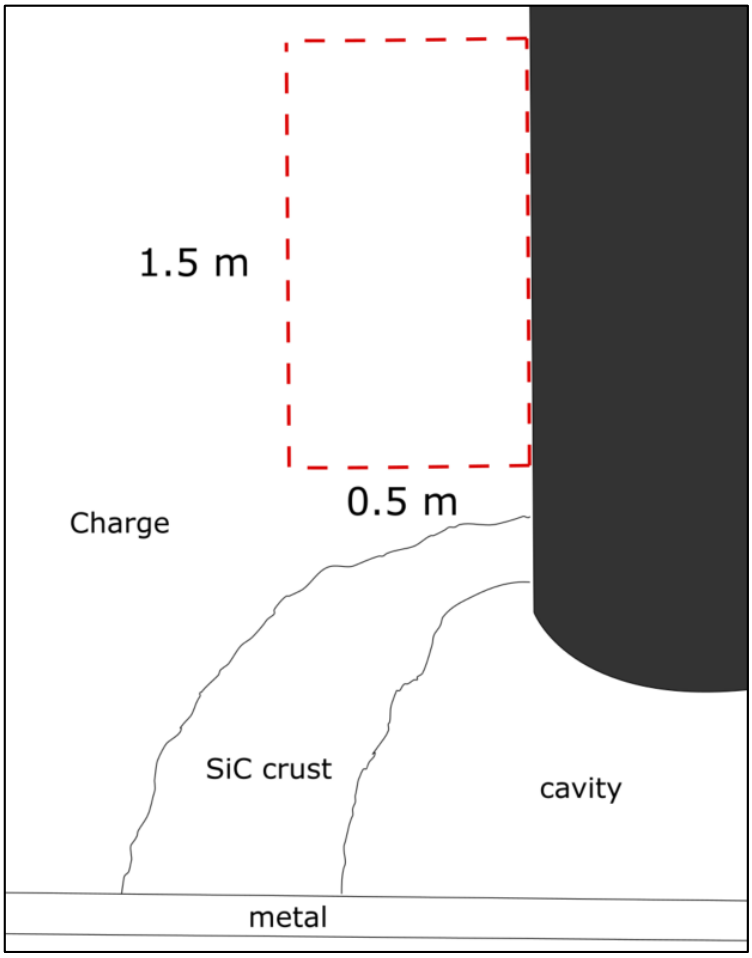

Figure 3.1: Illustration of the inner structure of a Si furnace. The area of charge material that is the basis for the geometry of the simulation is highlighted by the red dotted lines.

3.3 Calculation of Gas Volumes and Gas Velocities

The calculations of gas volume and gas velocities were based on previous calculations done by Tveit [45]. The volume of the gas is calculated by assuming an ideal gas. As for the geometry of the upscaled experiments, the gas velocities are based on a 45 MW furnace with three 1700 mm diameter electrodes. The calculations of produced gass were based on equation (2.14) with the silicon yield of the production assumed to be 85 %.

$$SiO_2 + (1+x)C = xSi + (1-x)SiO + (1+x)CO \tag{2.14}$$

The mass and volume of the different gas species produced per hour is given in Table 3.2.

Table 3.2: Mass CO gas and SiO gas produced per hour in a 45 MW furnace [45].

Specie	***Mass produced***	***Volume produced***
$CO_{(g)}$	*9 130 kg/h*	*7 350 Nm^3/h*
$SiO_{(g)}$	*1 165 kg/h*	*592 Nm^3/h*
Total		*7 942 Nm^3/h*

70 % of the gas is assumed to rise within the area 1 m from the electrode. This is calculated as the area of a circle with diameter 2.7 m and subtracting the area of the electrode which is a circle of diameter 1.7 m. The active area around each of the electrodes is found to be 3.454 m^2, giving a total active area of 10.362 m^2.

For the simulation the temperatures of interest are 1750 °C, 1400 °C, and 700 °C. The gas volumes at these temperatures are calculated by use of the ideal gas law and multiplying by 70 % which is how much of the gas is assumed to rise within the active area. The velocity in m/s is found by dividing the gas volume by the active area and is given in Table 3.3.

Table 3.3: Gas volume and velocity at different temperatures.

Temperature	***Gas Volume***	***Gas Velocity***
1750 ℃	*11.44 m^3/s*	*1.10 m/s*
1400 ℃	*9.46 m^3/s*	*0.91 m/s*
700 ℃	*5.50 m^3/s*	*0.53 m/s*

3.4 Modelling

The cases studied in this thesis were simulated using OpenFOAM. Two different solvers were used: *porousSimpleFoam* for incompressible flow, and *rhoPorousSimpleFoam* for compressible flow. Both solvers are steady-state solvers for turbulent flow through porous media. The solvers solve the Navier-Stokes equations, in the incompressible form for the incompressible solver and in the general form for the compressible solver with Darcy-Forchheimer added as a sink term.

The simulations were run on a Hp ENVY laptop with 4GB RAM and a Intel i3-7100U CPU (2.4 GHz).

3.4.1 Base Cases

Tutorial cases for the different solvers are used as base cases to ensure the file structure of the case is correct for the solver. The tutorial case used for the incompressible solver, porousSimpleFoam, was copied from the foam tutorials, at the location:

```
$FOAM_TUTORIALS/incompressible/porousSimpleFoam/angledDuctImp
licit
```

The tutorial case used for the compressible solver, rhoPorousSimpleFoam, was coped from the foam tutorials at the location:

```
$FOAM_TUTORIALS/compressible/rhoPorousSimpleFoam/angledDuctIm
plicit
```

Neither the tutorial case for the porousSimpleFoam solver nor the tutorial case for the rhoPorousSimpleFoam solver included a geometry for the simulation. The same geometry was used for both base cases and was copied from:

```
$FOAM_TUTORIALS/resources/blockMesh/angledDuct
```

The geometry was copied to a *blockMeshDict* file in the system folder.

3.4.2 Parameters Set for the Simulations

Parameters set in the *controlDict* is given in Table 3.4 for both the incompressible and the compressible cases.

Table 3.4: Parameters set in the controlDict for the simulations of both the incompressible and the compressible cases.

Parameter	***Setting, incompressible***	***Setting, compressible***
application	*porousSimpleFoam*	*rhoPorousSimpleFoam*
startTime	*0*	*0*
endTime	*5000*	*5000*
deltaT	*1*	*1*
writeInterval	*100*	*100*

The *application* is choice of solver used, *startTime* is when the simulation starts usually set to 0, *endTime* is the time step where the simulation finishes, *deltaT* is the size of the time steps, and *writeInterval* is how often the calculated solutions for the time steps are written to file. The end time for the simulation was set arbitrary high to allow the simulations to converge. If the solution has converged at an earlier time step, the simulation ends earlier.

The tolerances and relaxation factors set in *fvSolution* are given in Table 3.5.

Table 3.5: Tolerances and relaxation factors used for the simulations.

Variable	***Tolerance***	***Relaxation factor***
p	*1e-08*	*0.3*
U	*1e-07*	*0.7*
k	*1e-07*	*0.9*
epsilon	*1e-07*	*0.9*

The solution process is an iterative process meaning that they are based on reducing the residual over successive solutions. This residual is a measure of the error in the solution, and the *tolerance* represents the level at which the residual is small enough that the solution is sufficiently accurate. The *relaxationFactors* control the under-relaxation, which is a technique

used to improve the stability of a computation. This factor limits how much a variable can change from one iteration to the next, and is set to a number between 0 and 1. The relaxation factor should be small enough to ensure stable computation, but large enough to move the iterative process forward [46].

The initial values in the 0 directory that are identical for the incompressible and the compressible solvers are given in Table 3.6 and include velocity (*U*), the turbulent kinetic energy (*k*), turbulent kinetic energy dissipation rate (*epsilon*), and the turbulent kinematic viscosity (*nut*). The temperature is also set in the 0 directory and is set according to the given case being studied.

Table 3.6: Initial values for fields that are identical for the incompressible and the compressible solvers.

Field	***Value***	***Unit***	***Setting***
U	*0.03*	m^3s^{-1}	*No slip*
K	*1*	m^2s^{-2}	*initial*
epsilon	*200*	m^2s^{-3}	*initial*
nut	*0*	m^2s^{-1}	*uniform*

Initial values that are not identical for the incompressible and the compressible solvers are given in Table 3.7, and include initial pressure (*P*), and the turbulent thermal diffusivity, (*alphat*).

Table 3.7: Initial values for fields that are not identical for the incompressible and the compressible solvers.

Field	***Solver***	***Value***	***Unit***	***Setting***
P	*Incompressible, porousSimpleFoam*	*0*	m^2s^{-2}	*Zero gradient*
P	*Compressible, rhoPorousSimpleFoam*	10^5	*Pa*	*ZeroGradient*
alphat	*Compressible, rhoPorousSimpleFoam*	*0*	$kgm^{-1}s^{-1}$	*uniform*

Because the density is constant in the incompressible case, the pressure field is calculated as pressure divided by density, $\frac{p}{\rho}$, and has the unit m^2s^{-2}. The obtained pressure values from the simulation must be multiplied with the density of the fluid to obtain the pressure in *Pa*. The incompressible solver does only account for relative pressure and not total pressure. The initial value is thus not of importance for the simulation and is set to 0 to obtain the pressure difference directly.

For the compressible solver, the pressure is calculated in *Pa*. In this solver the total pressure is calculated, meaning atmospheric pressure plus the pressure difference caused by the resistance in the packed bed. The initial pressure is here set to atmospeheric pressure at 10^5 Pa. To obtain the pressure difference caused by the resistance in the packed bed the atmospheric pressure of 10^5 Pa needs to be subtracted from the resulting pressure field from the simulation. The compressible solver has an additional field containing the turbulent thermal diffusuvity, *alphat*. This is set to 0 in the simulations.

The physical properties of air at 25 °C, 700 °C, 1400 °C and 1750 °C are given in Table 3.8.

Table 3.8: Thermodynamic properties of air at 25 ℃, 700 ℃, 1400 ℃, and 1750 ℃ [47].

Property	***25 ℃***	***700 ℃***	***1400 ℃***	***1750 ℃***	***Unit***
Density	*1.184*	*0.363*	*0.262*	*0.177*	kg/m^3
Molecular weight	*28.9*	*28.9*	*28.9*	*28.9*	$gmol^{-1}$
Cp	*1005*	*1135*	*1224*	*1249*	$Jkg^{-1}K^{-1}$
Dynamic viscosity	*1.82*	*4.11*	*5.02*	*6.22*	$10^{-5}\ kgm^{-1}s^{-1}$
Kinematic viscosity	*0.156*	*1.133*	*2.686*	*3.596*	$10^{-4}\ m^2s^{-1}$
Pr	*0.71*	*0.71*	*0.73*	*0.75*	-

The physical properties of the system are defined in the *constant* directory. In *momentumTransport,* the model for momentum transport is set to Reynolds Averaged Simulations, RAS, which includes turbulent flow. This solution model for momentum transport can introduce turbulence to the system. If the flow is truly laminar this model will still converge and turbulence will not be introduced in the flow, but it might need more iteration steps to do so [48]. In the *porosityProperties* the Darcy-Forchheimer coefficients are set according to the packed bed being studied. For the incompressible cases the last file in the

constant directory is the file *transportProperties.* In this file the transport model is set to Newtonian.

For the compressible cases the last file in the *constant* directory is the file *thermophysicalProperties.* In this file the type of fluid is defined to *heRhoThermo*, which is a thermophysical model for fixed composition based on density [49]. The fluid is set to be a pure mixture and a perfect gas.

3.4.3 Simulating Small-Scale Cold Experiment

The first simulations will be of the small-scale cold experiments done previously by the author. In these experiments the boundary conditions and the expected pressure is known. The results from the simulations can thus be compared with the experimental results to validate the model.

The geometry and meshing of the simulations are given in Table 3.9.

Table 3.9: Geometry and meshing of the simulations for the small-scale cold experiments.

Parameter	***Length [mm]***	***Number of cells***
Width	*185*	*20*
Depth	*-*	*1*
Height inlet	*30*	*5*
Height porous zone	*700*	*300*
Height outlet	*10*	*5*

The geometry was set equal to the geometry of the cylinder in the experimental rig shown in Figure 2.10, with an inner diameter of 185 mm, a non-porous zone of 30 mm at the bottom below the packed bed and a porous zone of 700 mm height. Above the porous zone is a 10 mm outlet with no porosity that does not affect the pressure.

The geometry is created as three blocks: inlet, porosity zone, and outlet, where porosity properties can be added to the blocks. The geometry is defined with 20 cells in the y-direction which is the width of the packed bed. For the height of the cylinder there is set 5 cells in the inlet, 300 cells in the porous zone, and 5 cells in the outlet. Because the simulations are in 2D

the depth is not defined separately in the geometry. The depth of the geometry is set equal to the width but with the number of cells for calculations in this direction is set to 1, resulting in a 2D simulation.

The geometry and the meshing are shown in Figure 3.2. The total geometry is defined in the *blockMeshDict* which is given in the Appendix in C Geometry of Small-Scale Cold Experiment.

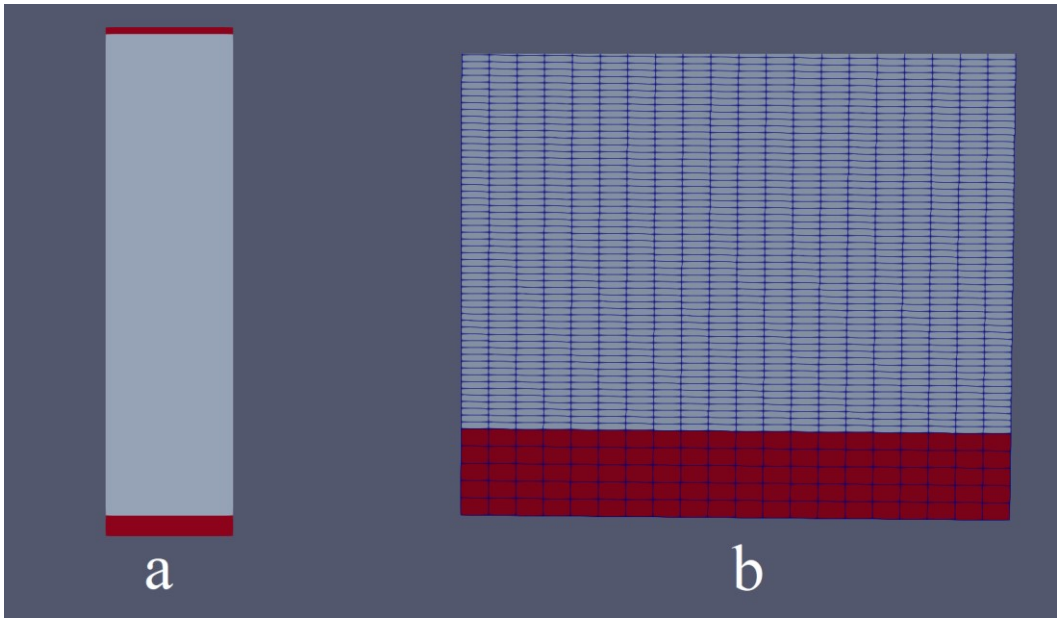

Figure 3.2: a) Geometry of the case for the small-scale cold experiment. b) Section of the lower part of the geometry enlarged to show the meshing.

All simulations done of the small-scale cold experiments are given in Table 3.10. All three cases were simulated at 25 °C, with both incompressible and compressible gas flow.

Table 3.10: List of simulations for the small-scale cold experiments. All cases were simulated with solvers for both incompressible and compressible gas flow.

Simulation	***Solver***	***Temperature [℃]***	***Case***
1	*Incompressible*	*25*	*1*
2	*Incompressible*	*25*	*2*
3	*Incompressible*	*25*	*3*
4	*Compressible*	*25*	*1*
5	*Compressible*	*25*	*2*
6	*Compressible*	*25*	*3*

3.4.4 Up-Scaling of Model to Simulate Furnace Conditions

To simulate gas flow through the charge in an industrial furnace the model was upscaled with basis in the theoretical silicon furnace of 45 MW with geometry as described in section 3 and gas velocities as described in 3.3. The parameters of the geometry and meshing for the up-scaled simulations are given in Table 3.11.

Table 3.11: Geometry and meshing of the upscaled simulations.

Parameter	***Length* [*mm*]**	***Number of cells***
Width	*500*	*30*
Depth	-	*1*
Height inlet	*1*	*1*
Height porous zone	*1500*	*600*
Height outlet	*1*	*1*

The geometry is defined with 30 cells in the y-direction which is the width of the packed bed. For the height of the geometry, the inlet and outlet are set to 1 mm each with 1 cell for the calculation as these parts are not of interest for the upscaled simulations. The porous media is set to 1500 mm in height with 600 cells. The depth of the geometry is set equal to the width but with the number of cells for calculations in this direction is set to 1, resulting in a 2D simulation.

The geometry and the meshing are shown in Figure 3.3 and Figure 3.4. The total geometry is defined in the *blockMeshDict* which is given in the Appendix in BGeometry of Upscaled Simulations with Furnace Conditions.

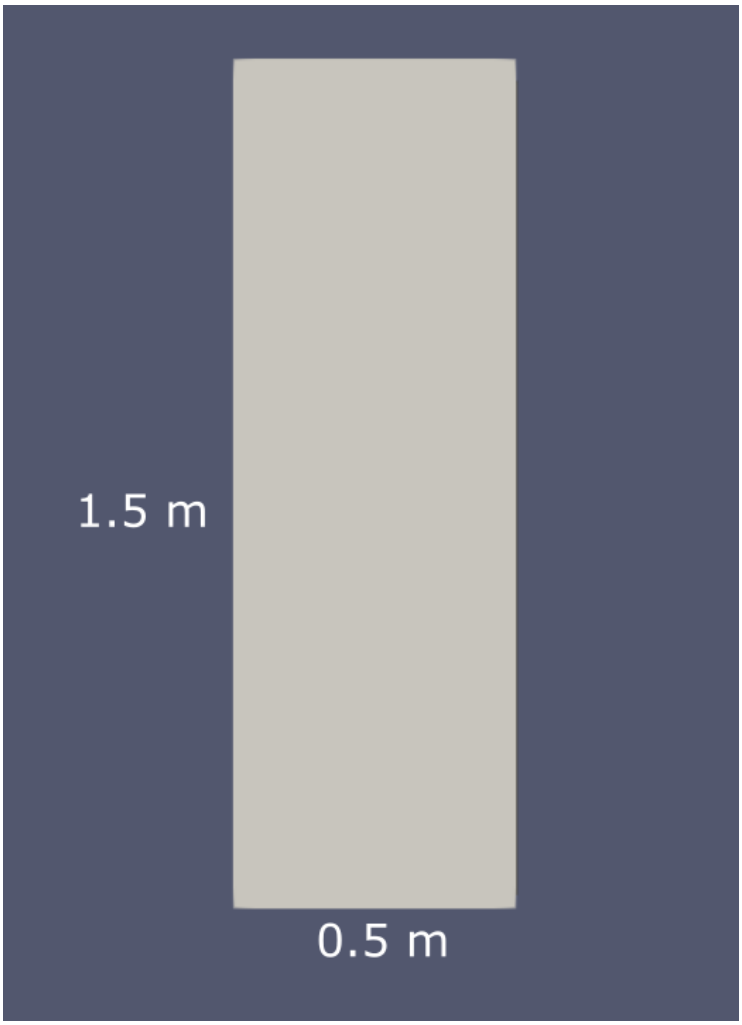

Figure 3.3: Geometry of the cases for the upscaled furnace conditions.

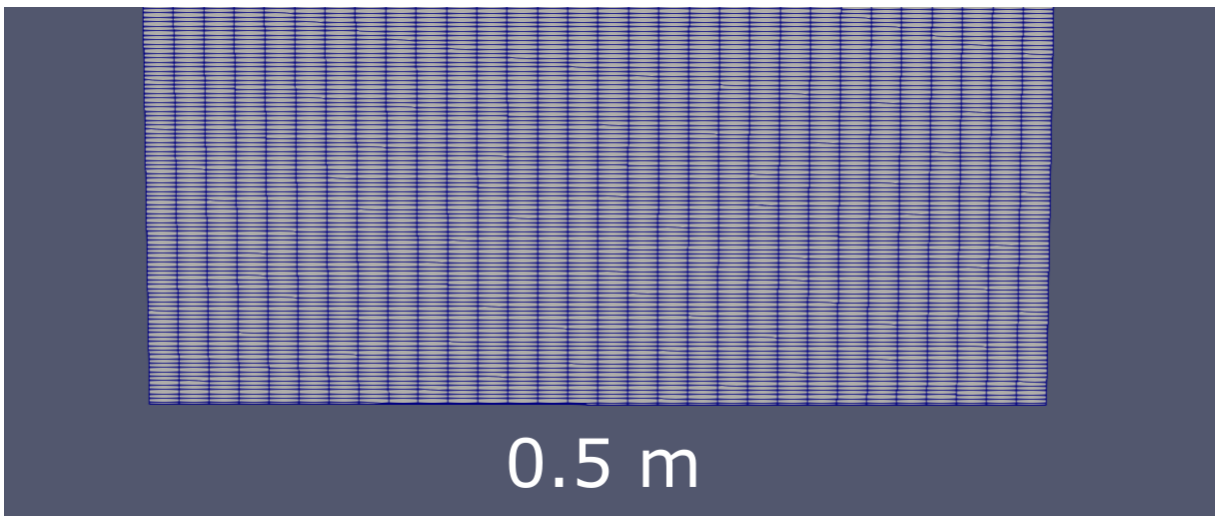

Figure 3.4: Meshing of the cases for the upscaled furnace conditions.

The simulation plan for all cases with upscaled furnace conditions is given in Table 3.12. All cases were simulated with both incompressible flow and compressible flow with the temperatures: 700 °C, 1400 °C, and 1750 °C. At 1400 °C, the gas velocity was also varied to study the effect of velocity as an independent variable.

Table 3.12: List of simulations for the upscaled conditions. All cases were simulated at the temperatures 1750 ℃, 1400 ℃, and 700 ℃, with solvers for both incompressible and compressible gas flow. At 1400 ℃ the gas velocity was varied.

Simulation	***Solver***	***Temperature [℃]***	***Velocity [m/s]***	***Case***
1	*Incompressible*	*1750*	*1.104*	*1*
2				*2*
3				*3*
4	*Compressible*	*1750*	*1.104*	*1*
5				*2*
6				*3*
7	*Incompressible*	*1400*	*0.912*	*1*
8				*2*
9				*3*
10	*Compressible*	*1400*	*0.912*	*1*
11				*2*
12				*3*
13	*Incompressible*	*700*	*0.532*	*1*
14				*2*
15				*3*
16	*Compressible*	*700*	*0.532*	*1*
17				*2*
18				*3*
19	*Incompressible*	*1400*	*1.104*	*2*
20			*0.532*	*2*
21	*Compressible*	*1400*	*1.104*	*2*
22			*0.532*	*2*

4 Results

Gas flow through porous media was simulated using OpenFOAM with the solvers *porousSimpleFoam* for incompressible flow and *rhoPorousSimpleFoam* for compressible flow. The results in this section include plots of the pressures obtained from simulations with different permeabilities, different temperatures, and different velocities at conditions based on a theoretical silicon furnace of 45 MW. The pressure field, a plot of the pressure and a plot of the velocity across the simulated area is also given for one of the incompressible and one of the compressible simulations. Results from simulation of previous experimental work with small-scale cold experiments will also be given in this section.

Three different permeabilities corresponding to three different particle sizes from previous experimental work was used in the simulations. The different permeabilities used are described as different cases where Case 1 has the lowest particle sizes with quartz at 0.25 – 2.00 mm and coal at 2.00 – 3.35 mm. Case 2 has particle sizes of quartz at 2.00 – 4.75 mm and coal from 5.00 mm to approximately 10 mm. Case 3 had a charge mixture of quartz at 2.00 – 4.75 mm, unsieved coal below approximately 10 mm and woodchips at 2 – 5 cm. The three cases are described in Table 3.1, in section 3.1 Choice of Cases and Parameters.

4.1 Pressure-Drop at Furnace Conditions at Different Temperatures

The pressure drop from gas flow through porous media was simulated through a charge material with dimensions 0.5 m in width and 1.5 m in height. The simulations were run with both incompressible and compressible gas flow for the three different cases at 700 °C, 1400 °C, and 1750 °C. For the simulations with compressible gas -low the velocity was not constant. Because of this variation in velocity the pressures from the incompressible simulations and the compressible simulations are not directly comparable at a given temperature, and they are thus presented in separate plots. The obtained pressure values from the simulations with incompressible gas flow is given for all three temperatures in Figure 4.1. The obtained pressure values from the simulations with compressible gas flow is given in Figure 4.2.

The highest pressures were obtained with the smallest particle sizes at Case 1 for both the incompressible and the compressible gas flow. For the simulations with incompressible gas

flow the highest pressure over all was obtained with Case 1 at 1400 °C, with a pressure of 33.3 kPa. For the simulations with compressible gas flow the highest pressure was obtained with Case 1 at 1750 °C, with a pressure of 30.8 kPa.

The simulations with Case 2 corresponding to a packed bed with quartz at 2.00 – 4.75 mm and coal at 5.00 – 10 mm, and Case 3 corresponding to a packed bed with quartz at 2.00 – 4.75 mm, coal below 10 mm, and woodchips at 2 – 5 cm resulted in a lower pressure compared with Case 1 which represents the packed bed with quartz at 0.25 – 2.00 mm and coal at 2.00 – 3.35 mm. In addition, Case 2 and Case 3 showed a low variability in pressure between the different simulations compared with Case 1.

For the simulations with incompressible gas flow the lowest pressures were obtained at 700 °C. The pressures at 1400 °C and 1750 °C gave quite similar results. For the simulations with compressible gas flow the obtained pressure showed an increase with increasing temperature with the lowest pressures at 700 °C and the highest pressures at 1750 °C.

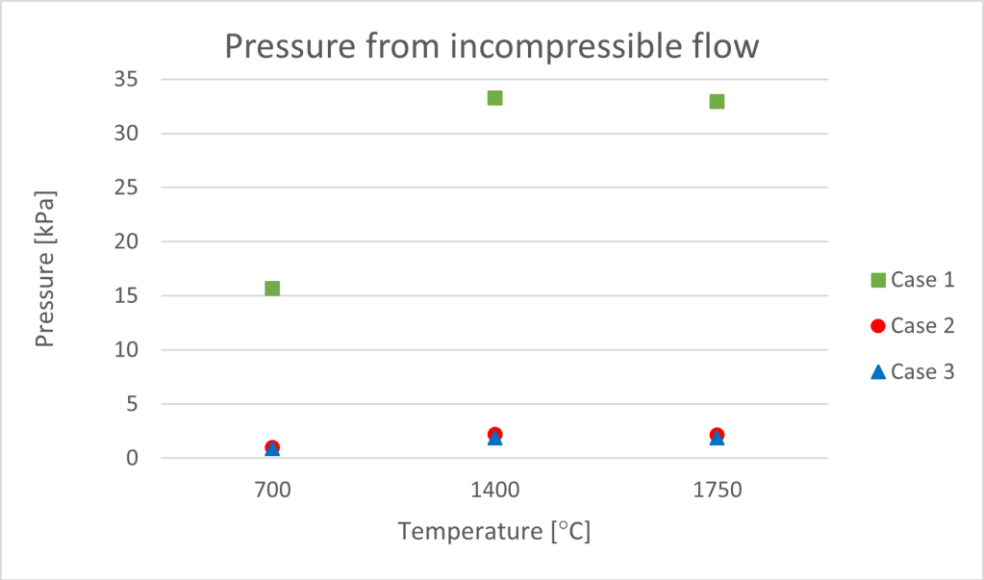

Figure 4.1: Pressure in kPa from simulations with incompressible flow for the three cases at different temperatures. The green indicators represent Case 1 (quartz at 0.25 – 2.00 mm and coal at 2.00 – 3.35 mm), the red indicators represent Case 2 (quartz at 2.00 – 4.75 mm and coal 5.00 – 10 mm), and the blue indicators represents Case 3 (quartz at 2.00 – 4.75 mm, coal below 10 mm, and woodchips at 2 – 5 cm.

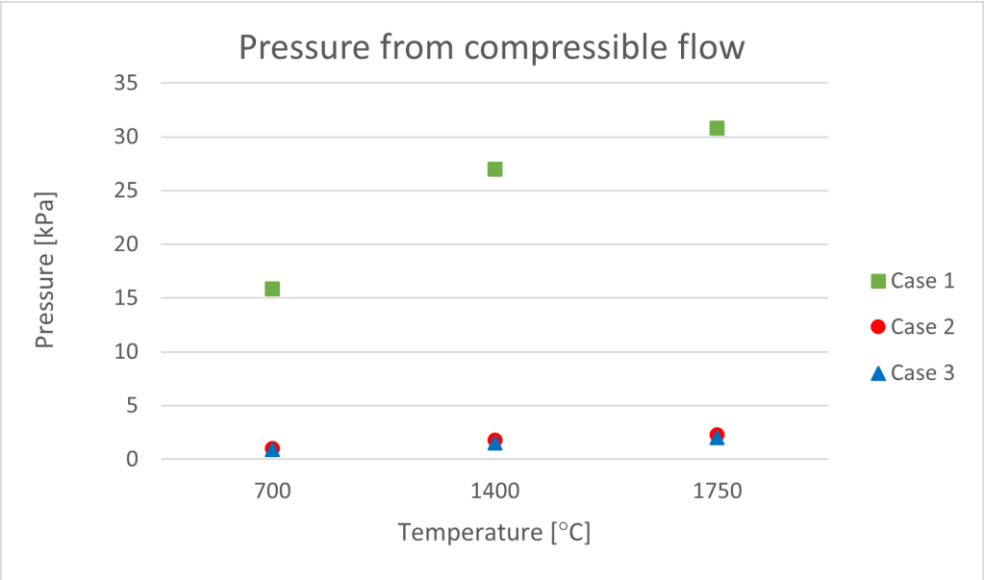

Figure 4.2: Pressure in kPa from simulations with compressible gas flow for the three cases at different temperatures. The green indicators represent Case 1 (quartz at 0.25 – 2.00 mm and coal at 2.00 – 3.35 mm), the red indicators represent Case 2 (quartz at 2.00 – 4.75 mm and coal 5.00 – 10 mm), and the blue indicators represents Case 3 (quartz at 2.00 – 4.75 mm, coal below 10 mm, and woodchips at 2 – 5 cm).

4.2 Pressure-Drop at Furnace Conditions with Varying Velocity

Gas flow through porous media was also simulated at a constant temperature of 1400 °C with the permeability of Case 2 at three different velocities, both with incompressible and compressible gas flow. The different velocities used was chosen to match the velocities at 700 °C and 1750 °C, to get comparable results. For the simulations with incompressible gas flow the velocities used were 0.532 m/s, 0.912 m/s, and 1.104 m/s. The simulations with compressible flow showed a small increase in velocity over the height of the simulated area. The velocities used for the compressible simulations were 0.53 – 0.54 m/s, 0.90 – 0.92 m/s, and 1.13 – 1.16 m/s. The pressure at the different velocities at 1400 °C is shown in Figure 4.3 for the incompressible simulations and in Figure 4.4 for the compressible simulations. Both the incompressible and the compressible simulations showed increasing pressure with increasing velocity.

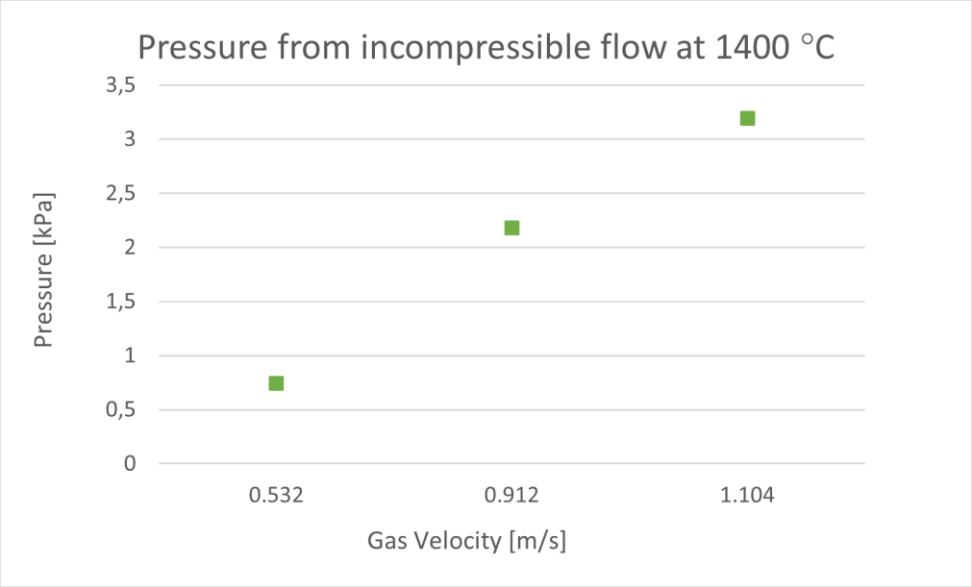

Figure 4.3: Pressure in kPa from simulations with incompressible gas flow and permeability of Case 2 with quartz at 2.00 – 4.75 mm and coal at 5.00 – 10 mm.

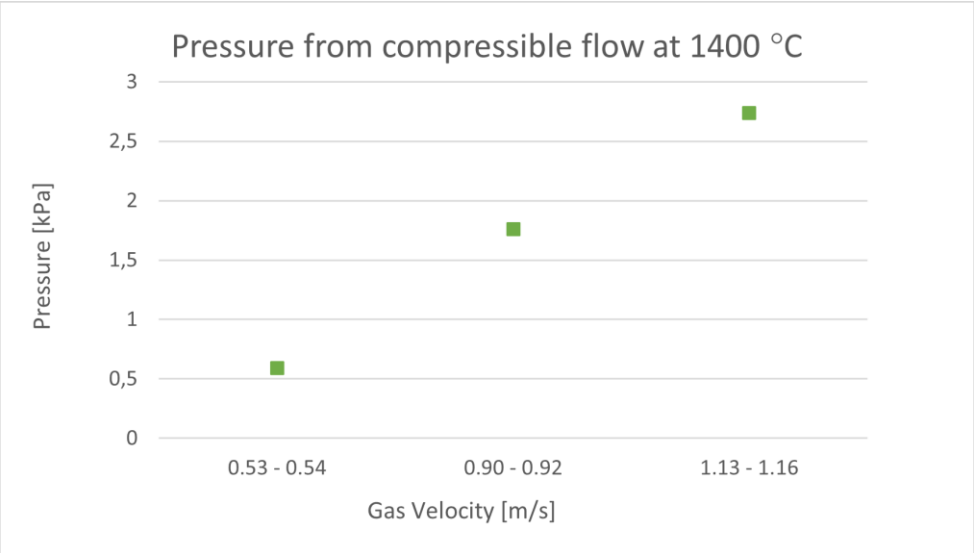

Figure 4.4: Pressure in kPa from simulations with compressible gas flow and permeability of Case 2 with quartz at 2.00 – 4.75 mm and coal at 5.00 – 10 mm.

4.3 Pressure Across the Simulated Area

All simulations resulted in a pressure field in the simulated area. An example of the pressure field from an incompressible simulation and the pressure field from a compressible simulation are shown in Figure 4.5. These pressure fields are from the simulations of Case 1 at 1750 °C. All simulations showed similar pressure fields with the highest pressures at the bottom and a gradually lower pressure toward the top.

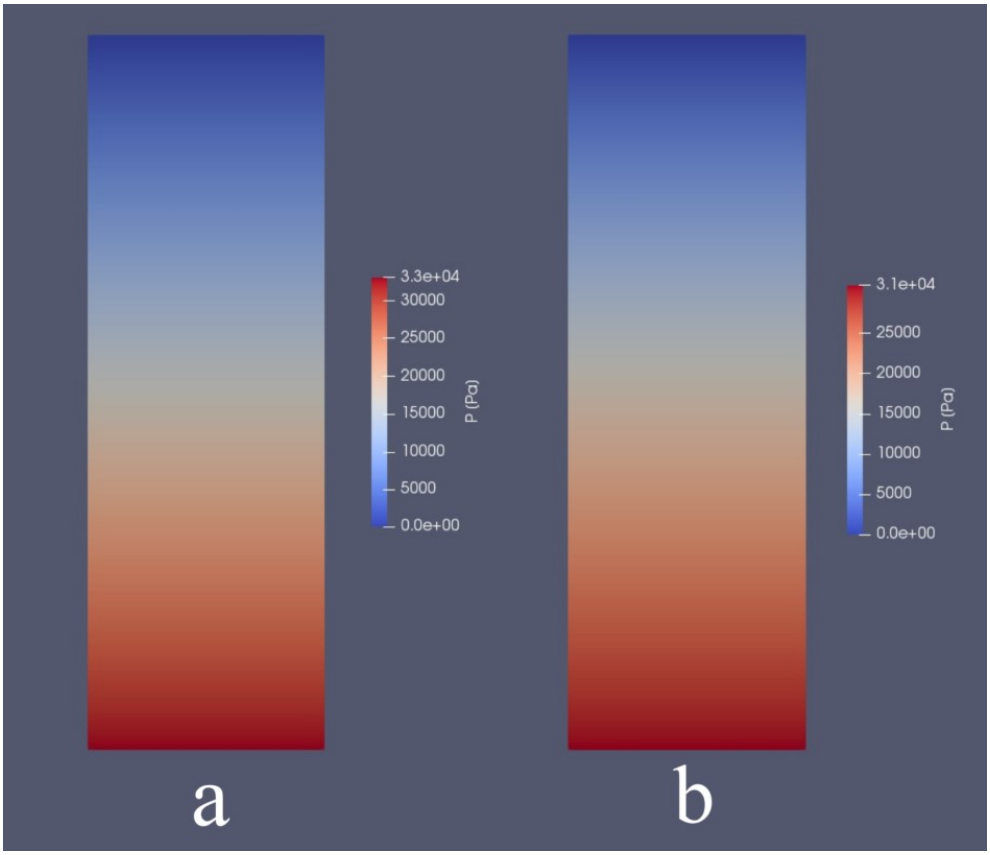

Figure 4.5: Pressure fields from the simulations of Case 1 at 1750 °C with a) incompressible gas flow and b) compressible gas flow.

Figure 4.6 and Figure 4.7 show the pressures plotted as a function of the height in the simulated area from the simulations of Case 1 at 1750 °C with incompressible and compressible gas flow. The height is the height of the simulated area where the pressure is the the build-up of pressure caused by the resistance in the porous media. The incompressible simulations showed a linear relationship between pressure and height. For the compressible simulations the pressure showed a slight positive deviation from linearity.

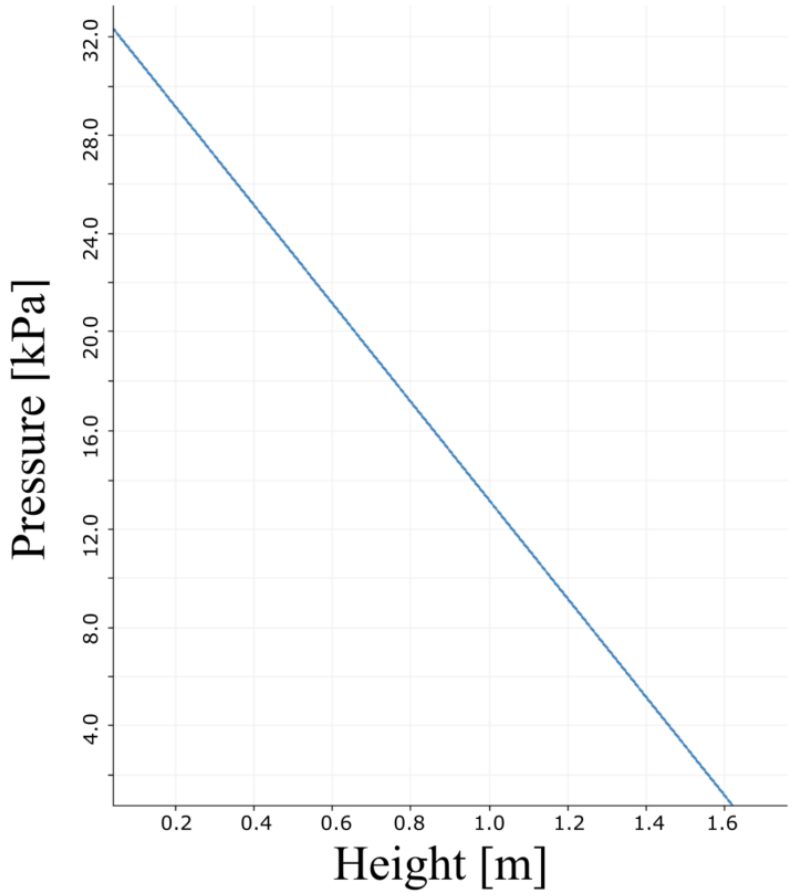

Figure 4.6: Pressure in kPa plotted against the height of the simulated area in m from the simulation of Case 1 at 1750 °C with incompressible gas flow.

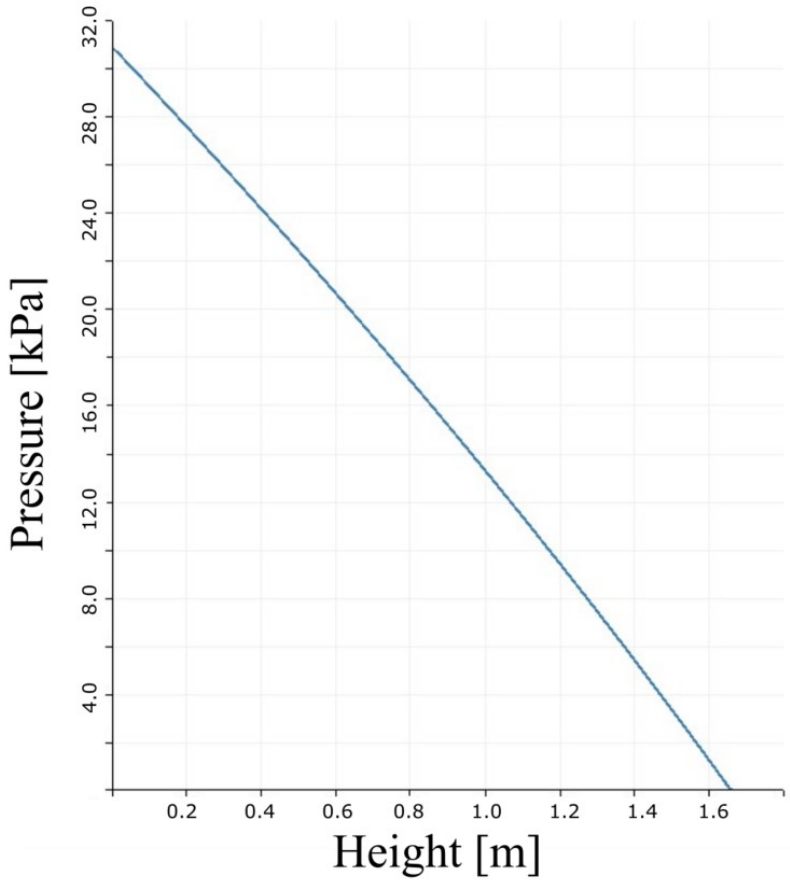

Figure 4.7: Pressure plotted against the height of the simulated area from the simulation of Case 1 at 1750 ℃ with compressible gas flow.

4.4 Velocity Across the Simulated Area

Figure 4.8 and Figure 4.9 show plots of the average velocity across the height of the simulated area from the simulations of Case 1 at 1750 °C with incompressible and compressible gas flow. The incompressible simulation showed a constant velocity across the entire simulated area. This was the case for all incompressible simulations. For the compressible simulation the velocity showed a slight increase with increasing height. The highest increase was seen at the highest velocity.

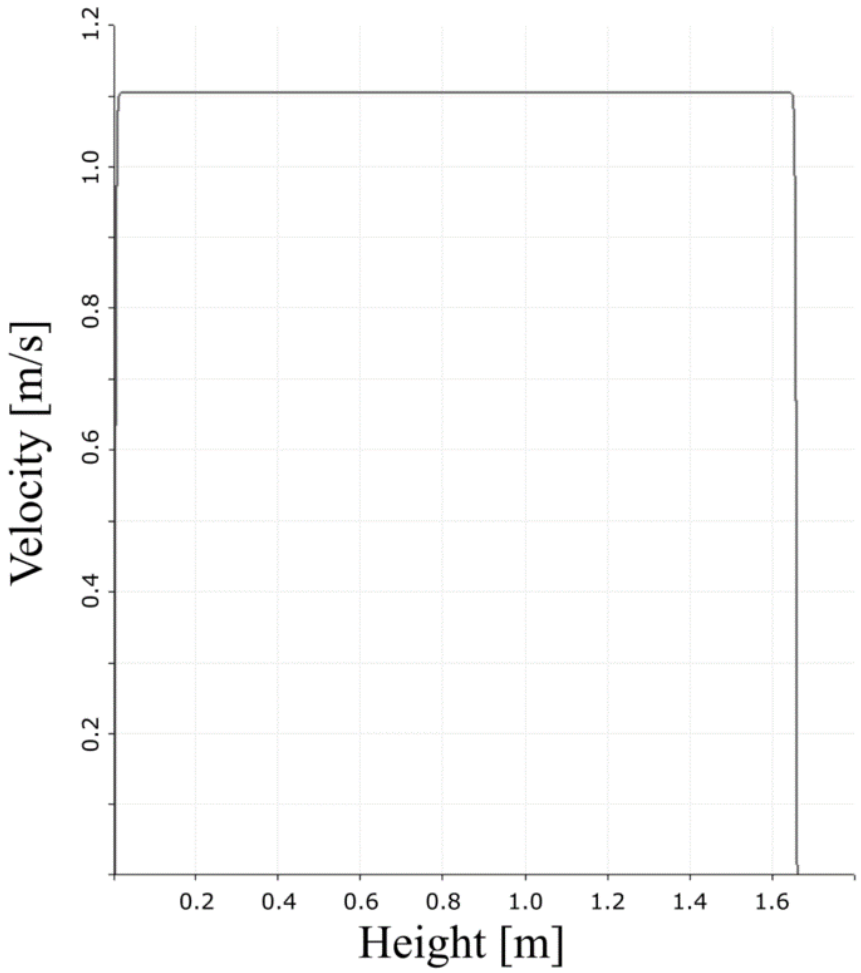

Figure 4.8: Velocity plotted against the height of the simulated area from the simulation of Case 1 at 1750 °C with incompressible gas flow.

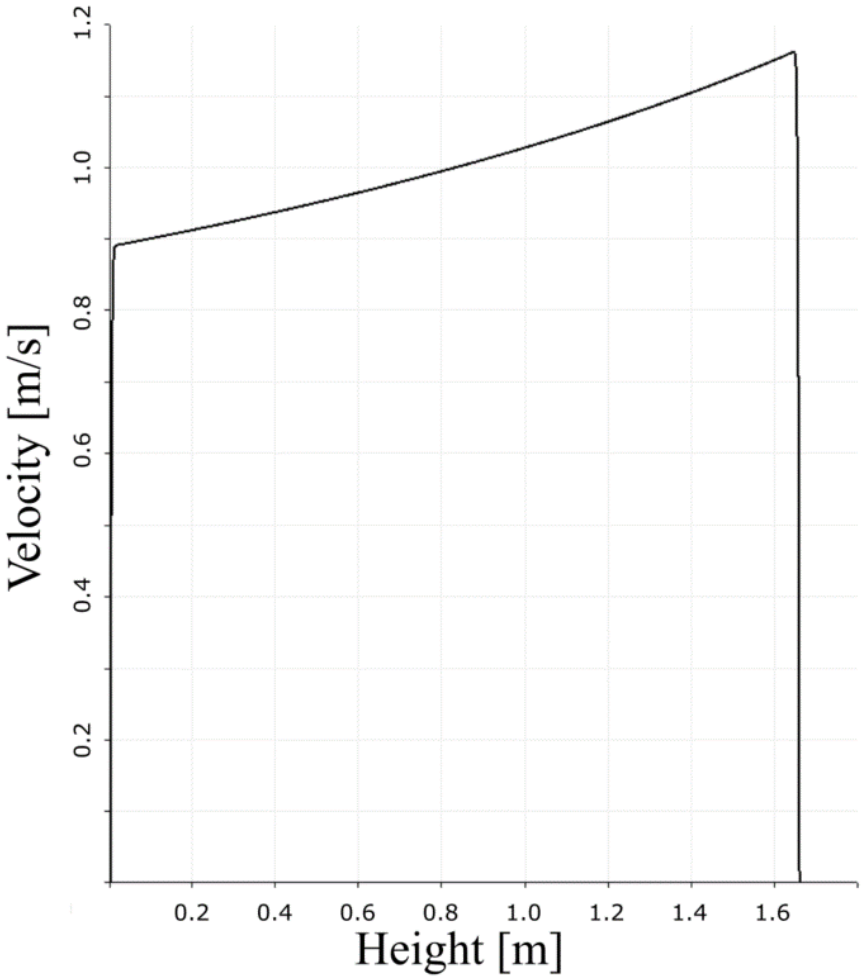

Figure 4.9: Velocity plotted against the height of the simulated area from the simulation of Case 1 at 1750 ℃ with compressible gas flow.

Because of this variation in velocity for the compressible simulations, the velocities had to be adjusted. For the simulations with compressible flow and varying temperature, the gas velocities were adjusted to fit the velocities of the incompressible simulations as best as possible. For the simulations with constant temperature at 1400 °C with varying velocity, the velocity of the compressible simulations was adjusted to match the velocities of the compressible simulations of Case 2 at 1750 °C and 700 °C. The velocities from the simulations with varying temperature is given for both incompressible and compressible gas flow in Table 4.1. The velocities from the simulations with temperature constant at 1400 °C is given in Table 4.2.

Table 4.1: Velocities from the simulations at the different temperatures for all three cases.

Temperature [℃]	***Case***	***Velocity, incompressible case [m/s]***	***Velocity, compressible case [m/s]***
1750	*1*	*1.104*	*0.89 – 1.16*
	2	*1.104*	*1.13 – 1.16*
	3	*1.104*	*1.13 – 1.16*
1400	*1*	*0.912*	*0.77 – 0.99*
	2	*0.912*	*0.90 – 0.92*
	3	*0.912*	*0.90 – 0.92*
700	*1*	*0.532*	*0.48 – 0.55*
	2	*0.532*	*0.53 – 0.54*
	3	*0.532*	*0.53 – 0.54*

Table 4.2: Velocities from the compressible simulations at 1400 ℃, where the velocity was varied.

Temperature [℃]	***Case***	***Velocity [m/s]***
1400	*2*	*1.13 – 1.16*
1400	*2*	*0.90 – 0.92*
1400	*2*	*0.53 – 0.54*

4.5 Simulations of Small-Scale Cold Experiments

Gas flow through porous media with the same geometry, permeability and boundary conditions as previous experimental work has been simulated both with incompressible and compressible gas flow. The resulting pressures at given velocities and permeabilities are shown in Figure 4.10 for the incompressible simulations and Figure 4.11 for the compressible simulations.

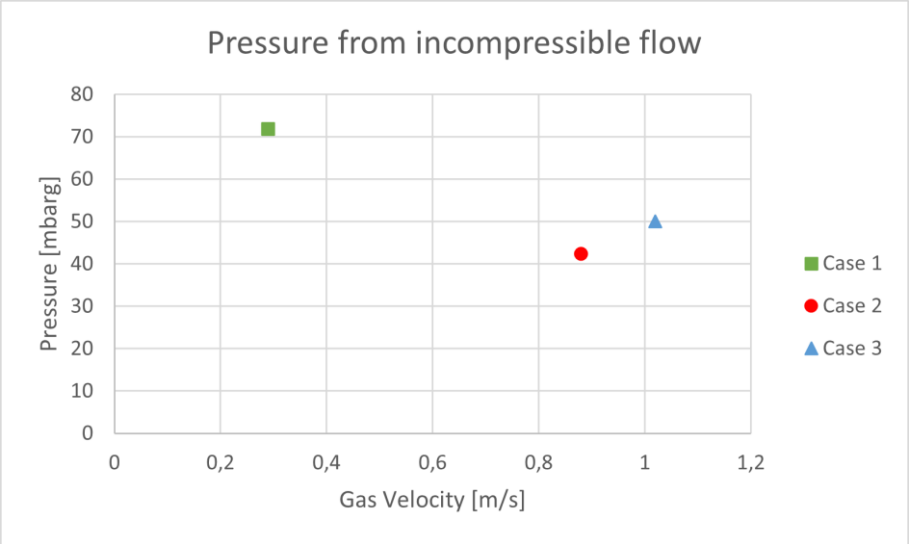

Figure 4.10: Pressures in kPa from the simulations of the small-scale cold experiment with incompressible flow. The green indicator represents the simulation of Case 1, the red indicator represents Case 2, and the blue indicator represents Case 3.

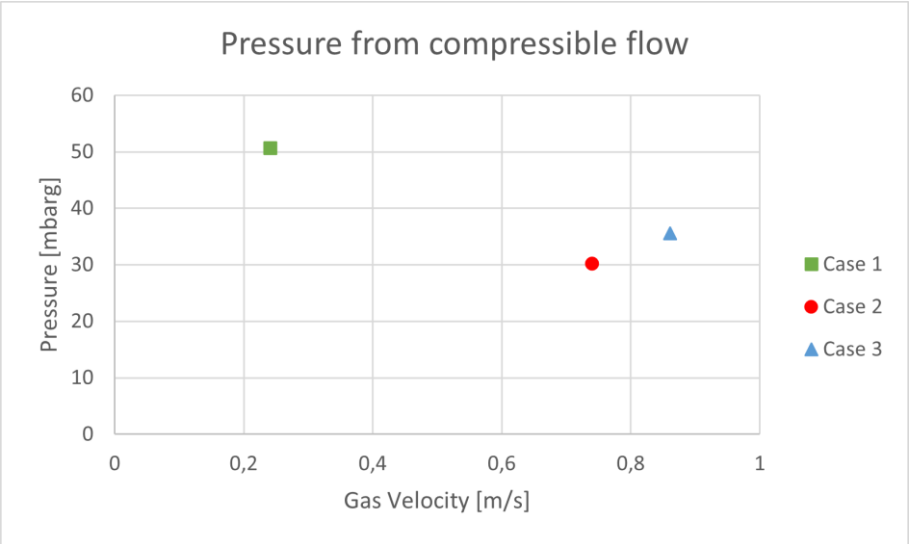

Figure 4.11: Pressures in kPa from the simulations of the small-scale cold experiment with compressible flow. The green indicator represents the simulation of Case 1, the red indicator represents Case 2, and the blue indicator represents Case 3.

5 Discussion

5.1 Effect of Particle Size

The particle size is studied through simulations of gas flow through porous media with different permeability based on experimental results of charge mixtures with different particle sizes. The effect of the particle size of coal has previously been studied by the author, and was found to have less of an impact on the build-up of pressure compared with the particle size of quartz, even with the smallest size fraction studied at 0 – 2.00 mm [6]. The effect of the particle size of coal is not studied further as a part of this thesis and is not included as a factor in the simulations. The focus in this discussion will therefore mainly be on the effect of the particle size of quartz.

The simulations of charge with quartz below 2.00 mm showed the highest pressures for all temperatures studied. These are the simulations of Case 1 with quartz at 0.25 – 2.00 mm and coal at 2.00 – 3.35 mm. Comparing the results it is apparent that the lowest pressure from all simulations with quartz below 2.00 mm is higher than the highest pressure of all simulations where quartz is above 2.00 mm. The simulations with quartz above 2.00 mm are the simulations of Case 2 with quartz at 2.00 – 4.75 mm and coal at 5.00 – 10 mm and of Case 3 with quartz at 2.00 – 4.75 mm, coal below 10 mm, and woodchips at 2 – 5 cm. The fact that quartz below 2.00 mm results in a higher pressure compared with quartz above 2.00 mm independent of the temperature and gas velocity indicates that the particle size, which in these simulations decides the permeability of the charge, is the most important parameter studied in regards of the build-up of pressure in the charge.

From earlier research done by the author it was found through experimental work that charge material with quartz particles below 2.00 mm had the greatest effect on pressure where a significant difference in pressure was found between charge mixtures with quartz above and below 2.00 mm. The results from the simulations in this thesis support this conclusion.

To study the effect of woodchips, the obtained pressures from Case 2 and Case 3 has been plotted without the results from Case 1. The pressures for Case 2 and Case 3 from the simulations with incompressible gas flow is given in Figure 5.1, and the pressure from compressible gas flow is given in Figure 5.2. From both the incompressible and the compressible simulations, the charge mixture with woodchips (Case 3) shows a lower

pressure compared with the charge mixture without woodchips (Case 2). This indicates that the addition of woodchips results in a lower build-up of pressure, and thus also a more even gas flow. This is as expected as the woodchips introduced voids and channels for the gas to flow through in the physical experiments. The difference between the pressures for Case 2 and Case 3 is however quite small, in the order of 200 – 300 Pa for both the incompressible and the compressible simulations. As the pressure in an industrial furnace has been measured to vary between 2 – 10 kPa, a difference of 200 – 300 Pa is not of significance [26].

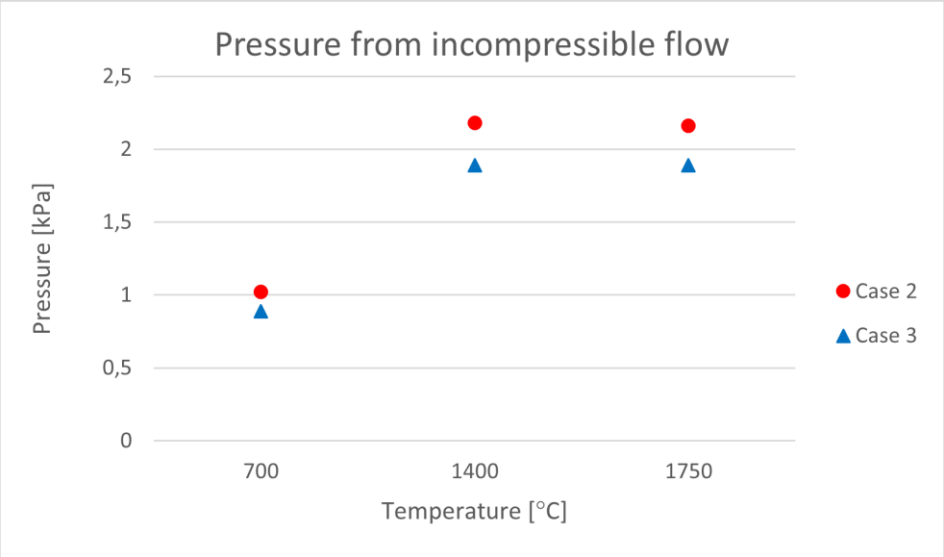

Figure 5.1: Pressure in kPa from Case 2 with quartz at 2.00 – 4.75 mm and coal at 5.00 – 10 mm, and Case 3 with quartz at 2.00 – 4.75 mm, coal below 10 mm, and woodchips at 2 – 5 cm, at different temperatures simulated with incompressible flow.

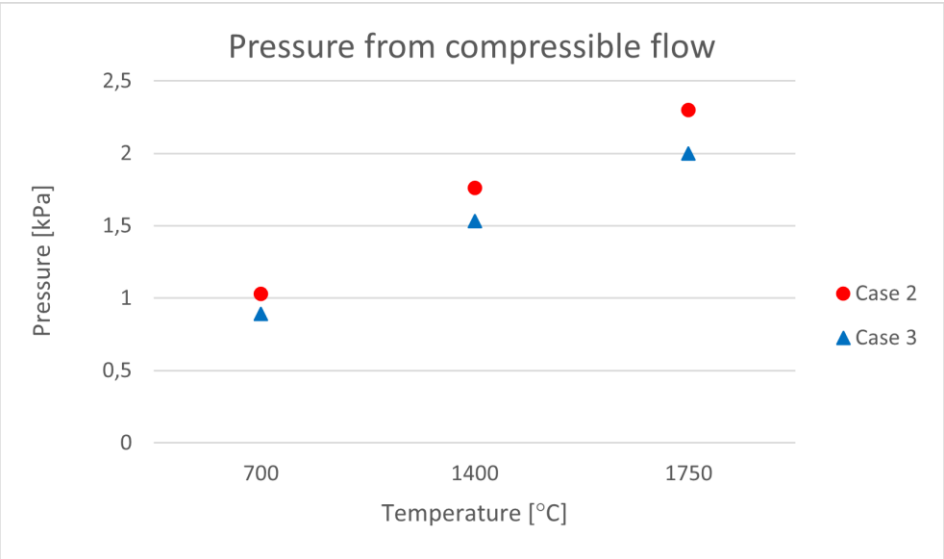

Figure 5.2: Pressure in kPa from Case 2 with quartz at 2.00 – 4.75 mm and coal at 5.00 – 10 mm, and Case 3 with quartz at 2.00 – 4.75 mm, coal below 10 mm, and woodchips at 2 – 5 cm, at different temperatures simulated with compressible gas flow.

5.2 Effect of Temperature and Gas Velocity

To study the effect of velocity, simulations were done at different velocities while keeping all other variables constant. The temperature was constant at 1400 °C, and the permeability was set constant by only studying Case 2. Figure 4.3 and Figure 4.4 show that the pressure increases with increasing velocity when all other parameters are unchanged. This result is as expected as the pressure from Darcy-Forchheimer, given in equation (2.18), is increasing with increasing velocity.

$$\frac{\Delta P}{\Delta L} = \mu \boldsymbol{D} V + \frac{1}{2} \rho \boldsymbol{F} V^2 \tag{2.18}$$

A Higher temperature results in the produced gas to have a higher gas volume, which again gives a higher gas velocity. As higher gas velocities result in higher pressures, a higher temperature will also generally result in higher pressures. However, by comparing the pressure results from the simulations at a constant temperature of 1400 °C, with the pressure results from the simulations at 700 °C and 1750 °C at the same velocities, the effect of temperature, excluding the effect on velocity, can be studied. This is effects caused by the temperature affecting the physical properties of the gas, such as density and viscosity. The pressures at given velocities with different temperatures are given in Figure 5.3 for incompressible flow and in Figure 5.4 for compressible flow.

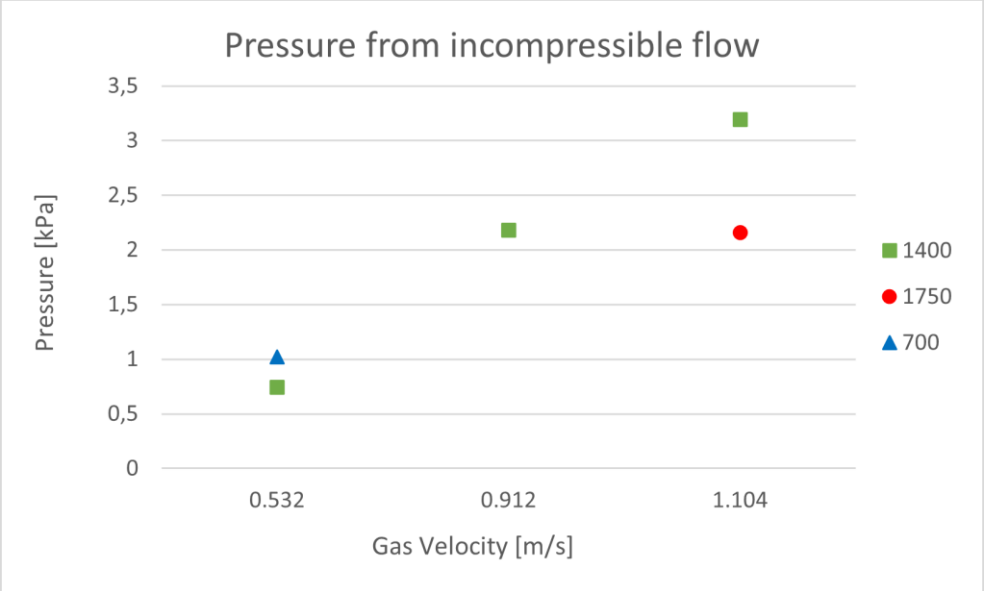

Figure 5.3: Pressure in kPa from simulations with incompressible gas flow and permeability of Case 2 with quartz at 2.00 – 4.75 mm and coal at 5.00 – 10 mm. The green indicators show the pressures at 1400 ℃, the blue indicator show the pressure from the simulation at 700 ℃, and the red indicator show the pressure from the simulation at 1750 ℃.

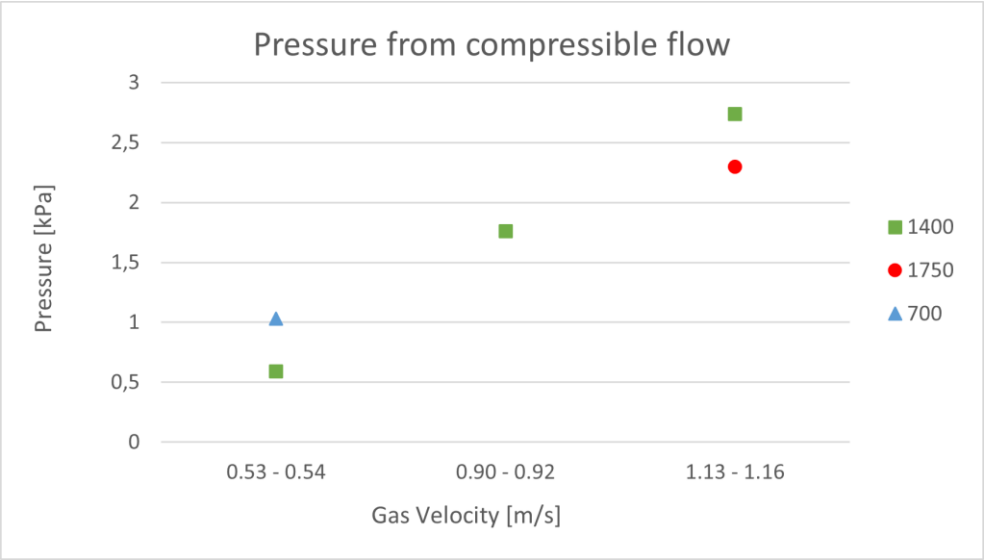

Figure 5.4: Pressure in kPa from simulations with compressible gas flow and permeability of Case 2 with quartz at 2.00 – 4.75 mm and coal at 5.00 – 10 mm. The green indicators show the pressures at 1400 ℃, the blue indicator show the pressure from the simulation at 700 ℃, and the red indicator show the pressure from the simulation at 1750 ℃.

Both Figure 5.3 and Figure 5.4 shows that the obtained pressure at the highest velocity was lower for the simulations at 1750 °C compared with the simulations at 1400 °C. For the lowest velocity the obtained pressure was lower for the simulations at 1400 °C compared with the simulations at 700 °C. This indicates that a higher temperature results in a lower pressure when the velocity is held constant.

Relating this to the silicon furnace this would mean that at the zones with higher temperatures, in addition to a greater gas volume resulting in a higher velocity and a higher pressure there will be an opposite effect from the physical properties of the gas resulting in a somewhat lower build-up of pressure.

5.3 Validation of Models

To validate the models used, small-scale cold experiments done previously was simulated. For these experiments all boundary conditions were known and the resulting pressure at a given velocity was measured for each charge mixture. The resistance in the charge was calculated by a regression of the measured pressures at different velocities and represented as the Darcy-Forchheimer coefficients. These coefficients were the basis for the simulations. The models used for the simulations are validated by comparing how well the resulting pressures at a given gas velocity match the experimentally measured pressure. As the Darcy-Forchheimer coefficients from the experimental regression is used in the simulations, this could cause a bias for the simulated pressures to match the regression line. The validation is thus not mainly to check if the Darcy-Forchheimer model is valid, but more to see if the pressure from gas flow through a charge with experimentally measured resistance can be simulated with Navier-Stokes equations with Darcy-Forchheimer as a sink term.

Simulations of three different experiments were done, referred to in this thesis as Case 1, Case 2, and Case 3. Case 1 corresponds to the experimental packed bed with quartz at 0.25 – 2.00 mm and coal at 2.00 – 3.35 mm. Case 2 corresponds to the experimental packed bed with quartz at 2.00 – 4.75 mm and coal at 5.00 mm to approximately 10 mm. Case 3 corresponds to the experimental packed bed with quartz at 2.00 – 4.75 mm, unsieved coal below approximately 10 mm, and woodchips in the size range 2 – 5 cm.

The results from both the incompressible and the compressible simulations are plotted with the estimated regression line from the previous experimental work in Figure 5.5, Figure 5.6, and Figure 5.7 for Case 1, Case 2, and Case 3 respectively. From the figures it appears that all the simulated pressures fit the regression line of the expected pressure from the experimental measurements quite well, both for the incompressible and the compressible model. This indicates that both the incompressible and the compressible model work well in predicting the gas flow and obtained pressures at the conditions corresponding to the experimental set-up.

The confidence intervals for the regression lines are calculated from the uncertainty in the measuring equipment and the variation between measurements at the same velocity from the experiments. As the Darcy-Forchheimer coefficients used for the simulations are taken from the regression line for the experimentally measured pressure, this uncertainty is also present in the simulations.

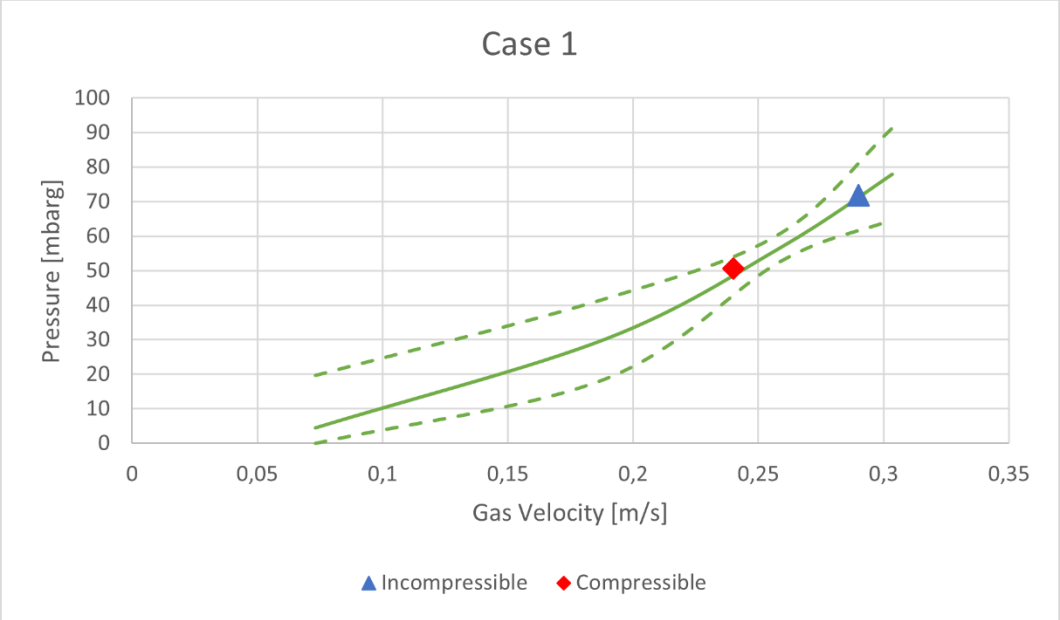

Figure 5.5: The indicators show the pressures from the incompressible (blue) and compressible (red) simulations for Case 1 with quartz at 0.25 – 2.00 mm and coal at 2.00 – 3.35 mm. The green solid line shows the estimated regression line from previous experimental work. The dotted lines show a 95 % confidence interval for the calculated regression line [6].

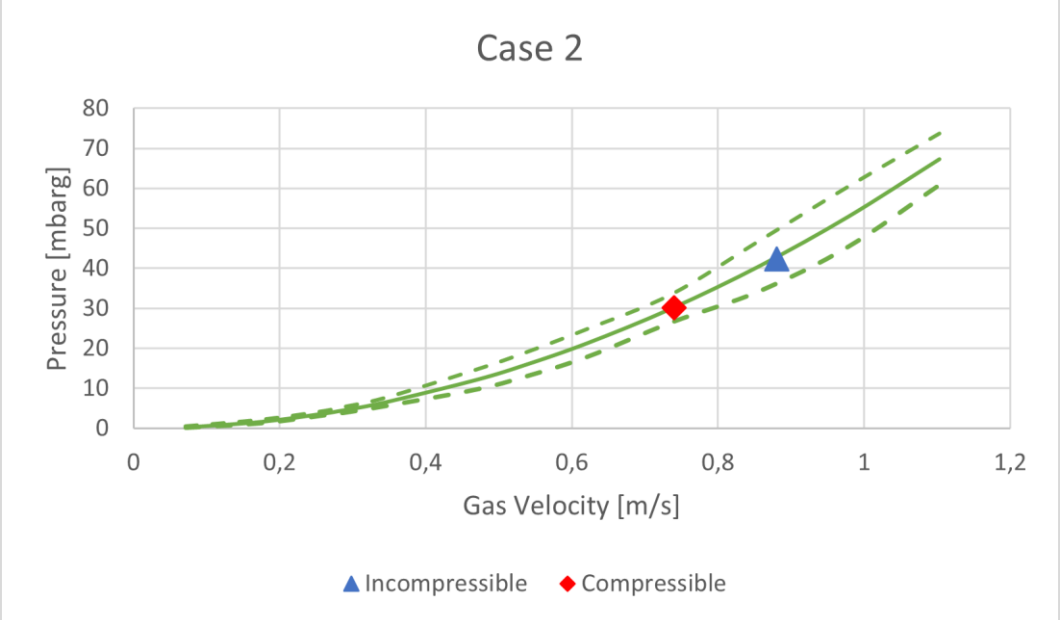

Figure 5.6: The indicators show the pressures from the incompressible (blue) and compressible (red) simulations for Case 2 with quartz at 2.00 – 4.75 mm and coal at 5.00 – 10 mm. The green solid line shows the estimated regression line from previous experimental work. The dotted lines show a 95 % confidence interval for the calculated regression line [6].

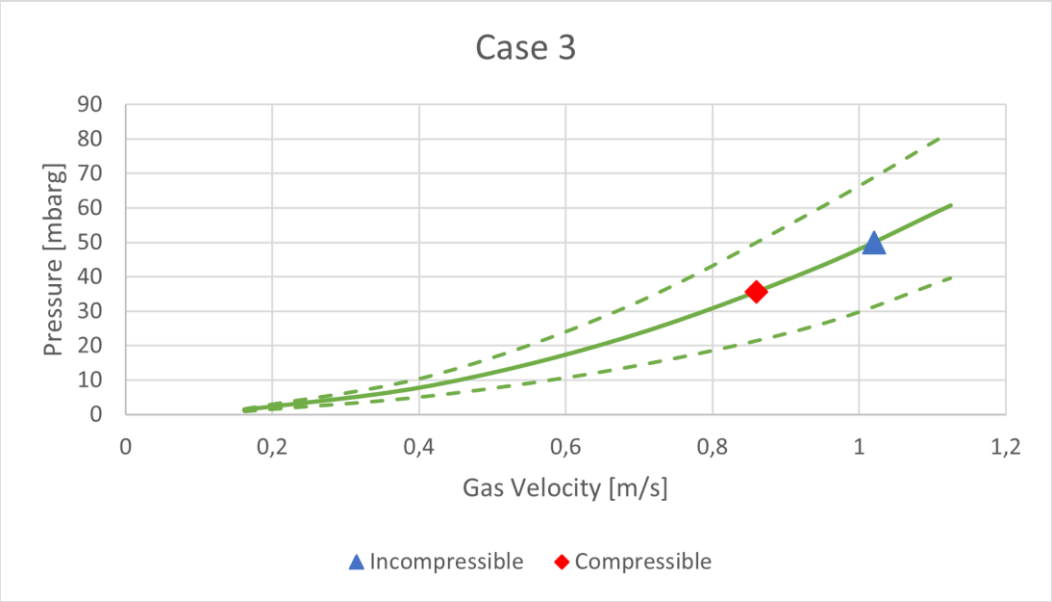

Figure 5.7: The indicators show the pressures from the incompressible (blue) and compressible (red) simulations for Case 3 with quartz at 2.00 – 4.75 mm, coal below 10 mm, and woodchips at 2 – 5 cm. The green solid line shows the estimated regression line from previous experimental work. The dotted lines show a 95 % confidence interval for the calculated regression line [8].

As the boundary conditions and obtained pressures are only known for the small-scale cold experiments, it is only possible to validate the model based on these conditions. For the simulations with upscaled conditions corresponding to a silicon furnace, all boundary conditions are estimations based on measurements from industrial furnaces and a geometry based on a theoretical 45 MW furnace with 1700 mm electrodes. The active area over which 70 % of the process gas flows is also an estimation. Because of the uncertainty in all the parameters of the upscaled simulations it is not possible to validate the model for these conditions. The validation is based on the small-scale cold experiments, and it is assumed that the model also can be used for upscaled geometry with other conditions.

5.4 Comparison of the Two Models Used

For the simulations in this thesis, there were found two different solution models that could be applied. The first model is an incompressible model, meaning that the density of the gas is set constant. For the specific cases in this thesis this also implies a constant velocity and a constant temperature. The second model used is a compressible model, where the density is not assumed to be constant. For this solution model it is possible with variation in both density, gas velocity, and temperature. If a gradient in temperature were to be implemented, the compressible model could still be used, in opposed to the incompressible model.

That the gas velocity for the incompressible simulations were constant across the simulated area can be explained from the continuity equation, (2.23), where for incompressible flow the total change in velocity has to be equal to zero to obey the governing equation of conservation of mass.

$$\nabla \boldsymbol{u} = 0 \tag{2.23}$$

The gas flow in these simulations is 2-dimensional with a geometry restricting flow in horizontal direction (*y*-direction). Because of this there can be local change in velocity in *y*-direction, but no global change. This means that the global change in *y*-direction, $\frac{dv}{dy}$, is zero. As the total change in velocity has to be zero for conservation of mass this implies that the global change in velocity in vertical direction (*x*-direction) also has to be zero, resulting in constant velocity.

As the density of a gas is coupled with the temperature, assuming incompressible flow also means that the system is assumed to be isothermal. If a temperature gradient were to be implemented into the simulation, this model could not be used.

For the compressible model, the velocity is not constant across the simulated area. In this model the density is not set to be constant and can thus vary. The continuity equation for compressible flow is given in equation (2.21).

$$\frac{d\rho}{dt} + \nabla(\rho \boldsymbol{u}) = 0 \tag{2.21}$$

As the simulation is steady state in 2-dimensions with no velocity in *y*-direction, this equation can in our case be simplified to:

$$\rho \frac{\partial u}{\partial x} + u \frac{\partial \rho}{\partial x} = 0 \qquad (5.1)$$

From this equation it can be seen that a change in density results in a change in velocity in order to have conservation of mass.

The obtained pressure values from the simulations of both incompressible and compressible gas flow are plotted in Figure 5.8 for the smallest particle sizes studied with quartz below 2.00 mm (Case 1) and in Figure 5.9 for the simulations with quartz above 2.00 mm (Case 2 and Case 3). For lower velocities both the incompressible and the compressible models gives approximately the same results. At higher velocities, a slight variation between the obtained pressure values can be seen. The pressure is expected to show a correlation with velocity from the Darcy-Forchheimer equation, where a higher velocity results in a higher pressure. The results from the incompressible simulations show that the pressures at a velocity of 0.9 m/s is approximately the same as the pressures at a velocity of 1.1 m/s. This discrepancy could be due to this model only considering the change in kinematic viscosity and density as the temperature is changed. The compressible solutions showed a correlation between pressure and velocity as expected from the Darcy-Forchheimer equation. This could indicate that the compressible solution model is more stable at higher temperatures.

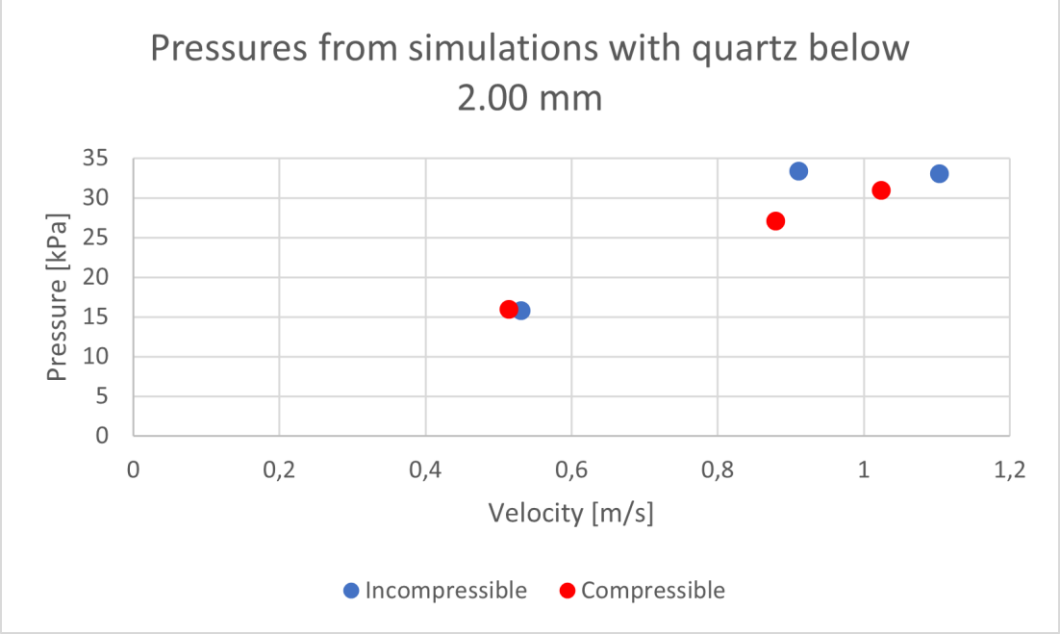

Figure 5.8: Pressures from simulation of packed beds with quartz at 0.25 – 2.00 mm and coal at 2.00 – 3.35 mm (Case 1). The red indicators represent the incompressible solutions, and the blue indicators represent the compressible solutions.

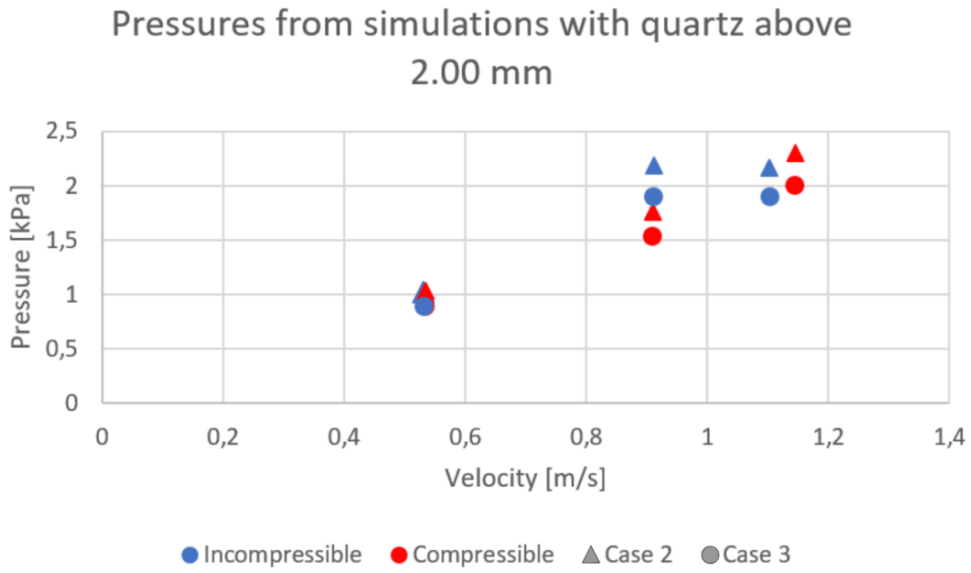

Figure 5.9: Pressures from simulation of packed beds with quartz at 2.00 – 4.75 mm and coal at 5.00 – 10 mm (Case 2), and quartz at 2.00 – 4.75 mm, coal below 10 mm, and woodchips at 2 – 5 cm (Case 3). The blue indicators represent the incompressible solutions, and the red indicators represent the compressible solutions. The triangular points are the pressures from Case 2 and the circular points are the pressures from Case 3.

For further research it could be considered using only one of the solvers. An assumption for the incompressible solver is that the density is constant over the entire area simulated. As the density is coupled with the temperature this also implies that the system is isothermal. Inside the silicon furnace there is a significant difference in temperature from the inner hot zone through the furnace to the upper zones with lower temperatures. The assumption of isothermal conditions can thus be valid only for small volumes. In addition, the isothermal model showed some deviation from the Darcy-Forchheimer equation at higher temperatures. For further investigations on the subject, it would thus be recommended to use the compressible solver as this model showed to be more consistent with the theory, and it allows for simulations with varying temperatures.

5.5 Pressure-Drop in Industrial Furnaces

An even gas flow in the silicon furnace is important to get stable processes in the furnace. A build-up of pressure in the furnace is caused by the resistance to gas flow from the lowered permeability of the charge. The permeability is lowered by various reasons including the creation of a dense condensate layer, the melting of the materials, the formation of fines, and the packing of the materials. An increased pressure may cause different operational problems including outbursts of gas and channel formation through the charge, and problems during tapping where you get gassing from the taphole.

The higher peaks of the measured pressure in an industrial silicon furnace has been found to not be caused by the packing of raw materials, but is most likely caused by the condensation of SiO clogging the charge [17]. Neither the effects of condensation of SiO, nor the effect of melting of the raw material is included as a part of the investigations for this thesis. These are effect which are not suitable to study through small-scale, experimental work. For this reason, only the effect of particle size, temperature, and gas velocity has been studied in this thesis.

Pressures in the crater has been measured at industrial silicon furnaces both at Elkem Thamshavn where the pressure was found to vary between 1 and 15 kPa and by researchers from Icelandic Alloys where the pressure was found to wary between 2 and 10 kPa [15], [26]. The obtained pressures from the simulations in this thesis, especially for the cases with quartz in the size range 0.25 – 2.00 mm and coal at 2.00 – 3.35 mm has values exceeding 15 kPa. For these cases the obtained pressure values vary from 15 – 33 kPa. Because of different assumptions used for the simulations, the results cannot be directly applied and compared with industrial conditions. For the simulations it has been assumed both isothermal conditions and constant permeability across the simulated area with a height of 1.5 m. In the simulations with incompressible gas flow it has also been assumed a constant density, which also implies a constant gas velocity. The charge materials studied also has a relatively low permeability and small particle sizes compared with the raw materials added to the furnace for silicon productions. Even though fines are produced in an industrial furnace, it is not expected to find larger zones consisting of only smaller particles which is the case for the simulations. The results from the simulations in this study is thus meant to be used as a parametric study, giving information about the effect of particle sizes, temperature, and gas velocity.

The simulations done for this thesis are based on a 45 MW silicon furnace with three 1700 mm electrodes. The results from the simulations done for this thesis have shown that charge material with quartz above 2.00 mm, has a low effect on the build-up of pressure in the furnace. These are the simulations of quartz in the size fraction 2.00 – 4.75 mm and coal at 5.00 – 10 mm (Case 2) and quartz at 2.00 – 4.75 mm, coal below 10 mm, and woodchips at 2 – 5 cm (Case 3). Quartz above 2.00 mm should thus from the results of these simulations, not cause a significant rise in pressure.

The simulations of gas flow through charge material with quartz below 2.00 mm resulted in high build-up of pressure for all velocities and temperatures studied. These are the simulations of quarts at 0.25 – 2.00 mm and coal at 2.00 – 3.35 mm (Case 1). The temperature and the velocity of the gas in an industrial furnace is highly dependent on the height in the furnace with the highest temperature and velocities closer to the electrodes and a lower velocity and temperature further up in the charge. This means that in regards of an industrial furnace, a layer with a permeability similar to that of the case with quartz below 2.00 mm would cause a distinct rise in pressure regardless of where in the furnace this layer is located. To achieve an even gas flow in the furnace it would thus be beneficial to minimize the amount of quartz fines below 2.00 mm in the furnace.

The quartz material that is added to the furnace in the silicon production is in the size order of approximately 10 – 150 mm [1]. As quartz with particle sizes above 2.00 mm showed a significantly lower build-up of pressure compared with quartz below 2.00 mm, the possibility of adding quartz at a lower particle size than 10 mm could be considered. With quartz added to the furnace being above 10 mm, the quartz below this size must be removed by sieving. The quartz below 10 mm is thereby not used for the silicon production and can be considered a waste product. If quartz at lower particle sizes could be used, for instance if the quartz could be sieved at 5 mm instead of 10 mm, considerably more of the quartz could be used for silicon production. This would be beneficial regarding a better utilization of resources and lowering the waste streams, which is important factors in regards of the green transition. This could also be beneficial in an economical view, as a better utilization of the raw material lowers the total amount of raw material needed per ton produced silicon which consequently lowers the cost of raw materials per ton silicon produced.

6 Conclusion

The particle size of quartz was found to be the most important of the parameters studied in this thesis in regards of the build-up of pressure in the silicon furnace.

Quartz with particle sizes above 2.00 mm was found to have a low effect on pressure and should thus not cause a significant rise in the pressure in the furnace. The possibility of adding quartz below 10 mm could thus be considered to get a better utilization of the raw material.

Quartz below 2.00 mm resulted in a high build-up of pressure for all velocities and temperatures studied. This indicates that a layer of charge material with quartz below 2.00 mm would cause a distinct rise in pressure regardless of where in the furnace this layer is located. It would thus be beneficial to minimize the amount of quartz below 2.00 mm in the furnace.

Addition of woodchips caused a lower build-up of pressure, and a more even gas flow. This effect was however low compared with the effect of the particle size of quartz.

The particle size of coal was studied in previous research and found to have a low effect on the pressure compared with quartz, even at particle sizes below 2.00 mm [6].

Both higher velocities and higher temperatures generally resulted in higher pressures. However, when keeping the velocity constant, a rise in temperature showed the opposite effect resulting in a somewhat lower build-up of pressure.

Two models were developed in OpenFOAM for simulating the gas flow through the charge in a silicon furnace. One model assumed incompressible gas flow where the density is constant and the other assumed compressible gas flow where the density was not assumed constant. Both models worked well in predicting the pressures from the previous small-scale cold experiments. The assumption of incompressible gas flow also implies constant gas velocity and constant temperature for the specific cases studied in this thesis. The incompressible model showed some deviation from theory at higher temperatures. For further investigation on the subject, it would therefore be recommended to use the compressible solver as this showed to be more stable at higher temperatures, and it allows for the implementation of varying temperatures.

7 References

[1] A. Schei, J. Kr. Tuset, and H. Tveit, *Production of High Silicon Alloys*. Trondheim, Norway: Tapir Forlag, 1998.

[2] "Silicon - Element information, properties and uses | Periodic Table." https://www.rsc.org/periodic-table/element/14/silicon (accessed Apr. 21, 2022).

[3] "Silicon in Electronics and Casting Applications." https://www.thomasnet.com/articles/chemicals/Silicon-Electronics-Casting-Applications (accessed Apr. 21, 2022).

[4] S. B. Norwegianscitechnews.com, "Silicon for solar cells becoming more environmentally friendly," *SINTEF*. https://www.sintef.no/en/latest-news/2021/silicon-for-solar-cells-becoming-more-environmentally-friendly/ (accessed Apr. 21, 2022).

[5] H. Edfeldt, "The Effect of Fine Material on Gas Flow in the Charge for Silicon Production," Department of Materials Science and Engineering, NTNU, Trondheim, Norway, Specialization Project, Fall 2018.

[6] A. Nordhus, "Gas Flow in Furnaces for Si Production," Department of Material Science and Engineering, NTNU, Trondheim, Norway, Specialization Project, Fall 2021.

[7] The OpenFOAM Foundation, *OpenFOAM*. OpenCFD Ltd.

[8] A. Nordhus, "Gas Flow Through the Charge in Silicon Production," SINTEF Industri AS, Trondheim, Norway, Summer 2021.

[9] *HSC Chemistry 9*. Outotec.

[10] M. Tangstad, *Metal Production in Norway*. Oslo, Norway: Akademika Publishing, 2013.

[11] M. Ksiazek *et al.*, "Industrial measurements of the gas and temperature in Si and FeSi production process (September 12, 2021)," Trondheim, Norway, Proceedings of the 16th International Ferro-Alloys Congress (INFACON XVI) 2021, Available at SSRN: https://ssrn.com/abstract=3922198 or http://dx.doi.org/10.2139/ssrn.3922198.

[12] E. Ringdalen, H. Tveit, S. Bao, and E. Nordnes, "Melting properties of quartz and their effect on industrial Si and FeSi production," Trondheim, Norway, Sep. 2019.

[13] W. D. Jr., Callister and D. G. Rethwisch, *Materials Scinence and Engineering*, 9. th. Wiley, 2015.

[14] D. Filsinger and B. Bourrie, "Silica to silicon: Key Carbothermic Reactions and Kinetics," J. Am Ceram Soc. 73[6]: 1726-32, 1990.

[15] H. Tveit, T. Halland, K. Landrø, S. T. Johansen, and B. Ravary, "The Tapping Process in Silicon Production," Silicon for the Chemical Industry VI, Trondheim, Norway, 2002.

[16] I. Brede, "Parameters Contributiong to the Formation of NOx in the Silicon Furnace," Department of Material Science and Engineering, NTNU, Trondheim, Norway, Master's thesis, Jun. 2013.

[17] H. Edfeldt, "Pressure drop in charge mixture in silicon production," NTNU, Department of Materials Science and Engineering, Trondheim, Norway, Master's thesis, Jan. 2020.

[18] K. F. Jusnes, "Phase transformations and thermal degradation in industrial quartz," Department of Material Science and Engineering, NTNU, Trondheim, Norway, Doctoral Thesis, Jun. 2020.

[19] K. Aasly, "Properties and Behaviour of Quartz for the Silicon Process," Department of Geology and Mineral Resources Engineering, NTNU, Trondheim, Norway, Doctoral Thesis, 2008.

[20] E. Ringdalen, "Quartz Properties in the FeSi/Si Process," presented at the Si Production Course, Oct. 05, 2021.

[21] A. Broggi, “Condensation of SiO and CO in silicon and ferrosilicon production,” NTNU, Department of Materials Science and Engineering, Trondheim, Doctorial thesis, Mar. 2021.
[22] G. Tranell, M. Andersson, E. Ringdalen, O. Ostrovski, and J. J. Steinmo, “Reaction Zones in a FeSi75 Furnace - Results from an Industrial Excavation,” *ISIJ Int.*, p. 8, 2010.
[23] Y. Otani, M. Saito, K. Usui, and N. Chino, “The Inner Structure in Submerged Arc Furnace,” Paper presented at the 6th International congress of electro heat, Brighton, England, 1968.
[24] M. Kadkhodabeigi, H. Tveit, and S. T. Johansen, “Modelling the Tapping Process in the Submerged Arc Furnaces Used in High Silicon Alloy Production,” ISIJ, 51(2), p 193., Trondheim, Norway, 2011.
[25] M. Ksiazek, M. Tangstad, and E. Ringdalen, “Five furnaces five different stories,” Presented at Silicon for the chemical and solar industry XIII, Kristiansand, 2016.
[26] H. T. Ingason, J. Halfdanarson, and J. A. Bakken, “Hollow Electrodes in the Production of FeSi75,” Presented at Infacon 7, Trondheim, Norway, 1995.
[27] H. Tveit, E. Ringdalen, and H. Edfeldt, “Important parameters that control the crater pressure in a Silicon Furnace,” Presented at Silicon for the chemical and solar industry XV, Trondheim, Norway, 2020.
[28] S. Grådahl, S. T. Johansen, B. I. Hop, and H. Tveit, “Miljø og ovnsprosesser. Del I.,” SINTEF Materialteknologi, Trondheim, Norway, 1997.
[29] K. Kadkhodabeigi, H. Tveit, and S. T. Johansen, “CFD modelling of the effect of furnace crater pressure on the melt and gas flows in the submerged arc furnaces used for silicon production,” *Prog. Comput. Fluid Dyn. Int. J.*, Sep. 2010.
[30] F. M. White, *Fluid Mechanics*, 7th. edition. McGraw-Hill, 2011.
[31] J. A. Bakken, “Metallurgical Engineering II, Fluid Flow and Heat Transfer, Advanced Course TMT4208.” Spring /2010 2009.
[32] S. Ergun, “Fluid Flow Through Packed Columns,” Chemical Engineering Progress, 1952.
[33] A. Bejan, “Convection heat transfer.” Wiley, New York, 1984.
[34] J. F. Wendt, J. D. Anderson, and Von Karman Institute for Fluid Dynamics, Eds., *Computational fluid dynamics: an introduction*, 3rd ed. Berlin ; [London]: Springer, 2008.
[35] H. E. Hafsteinsson, “Porous Media in OpenFOAM,” Chalmers University of Technology, 2009.
[36] “DarcyForchheimer - OpenFOAMWiki.” https://openfoamwiki.net/index.php/DarcyForchheimer (accessed May 03, 2022).
[37] B. Haddadi, C. Jordan, and M. Harasek, “OpenFOAM Basic Training.” chemical-engineering.at, Sep. 2019.
[38] G. Chen, Q. Xiong, P. J. Morris, E. G. Paterson, A. Sergeev, and Y.-C. Wang, “OpenFOAM for Computational Fluid Dynamics,” *Not. Am. Math. Soc.*, vol. 61, no. 4, p. 354, Apr. 2014, doi: 10.1090/noti1095.
[39] “OpenFOAM.” https://www.openfoam.com/ (accessed Mar. 16, 2022).
[40] “OpenFOAM: applications/solvers/incompressible/simpleFoam/porousSimpleFoam/porousSimpleFoam.C Source File.” https://cpp.openfoam.org/v9/porousSimpleFoam_8C_source.html (accessed Mar. 16, 2022).
[41] “OpenFOAM: applications/solvers/compressible/rhoSimpleFoam/rhoPorousSimpleFoam/rhoPorousSimpleFoam.C Source File.”

https://cpp.openfoam.org/v9/rhoPorousSimpleFoam_8C_source.html (accessed Mar. 16, 2022).
[42] C. Greenshields, “OpenFOAM v6 User Guide: 3.2 Compiling applications & libraries,” *CFD Direct*, Jul. 10, 2018. https://cfd.direct/openfoam/user-guide/v6-compiling-applications/ (accessed May 07, 2022).
[43] C. Greenshields, “OpenFOAM v8 User Guide: 4.1 OpenFOAM case directory,” *CFD Direct*, Jul. 21, 2020. https://cfd.direct/openfoam/user-guide/v8-case-file-structure/ (accessed May 07, 2022).
[44] “OpenFOAM: API Guide: kEpsilon< BasicTurbulenceModel > Class Template Reference.” https://www.openfoam.com/documentation/guides/latest/api/classFoam_1_1RASModels_1_1kEpsilon.html#details (accessed May 08, 2022).
[45] E. Ringdalen and H. Tveit, “Private Communication.” May 10, 2022.
[46] C. Greenshields, “OpenFOAM v6 User Guide: 4.5 Solution and algorithm control,” *CFD Direct*, Jul. 10, 2018. https://cfd.direct/openfoam/user-guide/v6-fvsolution/ (accessed May 09, 2022).
[47] “Viscosity of Air, Dynamic and Kinematic.” https://www.engineersedge.com/physics/viscosity_of_air_dynamic_and_kinematic_14483.htm (accessed May 09, 2022).
[48] “OpenFOAM: User Guide: Reynolds Averaged Simulation (RAS).” https://www.openfoam.com/documentation/guides/latest/doc/guide-turbulence-ras.html (accessed Jun. 02, 2022).
[49] C. Greenshields, “OpenFOAM v6 User Guide: 7.1 Thermophysical models,” *CFD Direct*, Jul. 10, 2018. https://cfd.direct/openfoam/user-guide/v6-thermophysical/ (accessed May 09, 2022).

Appendix

A Result from Simulations

The results from all simulations with upscaled conditions and information about the used temperature, solver, case, and velocity are given in Table A.1. The results from the simulations of the small-scale experiments and information about the solver, case, and velocity used are given in Table A.2.

Table A.1: All simulations done with upscaled conditions with temperature, solver, case, velocity, and resulting pressure.

Simulation	***Temperature* [°C]**	***Solver***	***Case***	***U* [*m/s*]**	***P* [*Pa*]**
1	*1750*	*Incompressible*	*Case 1*	*1.104*	*32970*
2	*1750*	*Incompressible*	*Case 2*	*1.104*	*2160*
3	*1750*	*Incompressible*	*Case 3*	*1.104*	*1890*
4	*1750*	*Compressible*	*Case 1*	*0.89 - 1.16*	*30830*
5	*1750*	*Compressible*	*Case 2*	*1.13 - 1.16*	*2300*
6	*1750*	*Compressible*	*Case 3*	*1.13 - 1.16*	*2000*
7	*1400*	*Incompressible*	*Case 1*	*0.912*	*33260*
8	*1400*	*Incompressible*	*Case 2*	*0.912*	*2180*
9	*1400*	*Incompressible*	*Case 3*	*0.912*	*1890*
10	*1400*	*Compressible*	*Case 1*	*0.77 - 0.99*	*26980*
11	*1400*	*Compressible*	*Case 2*	*0.90 - 0.92*	*1760*
12	*1400*	*Compressible*	*Case 3*	*0.91 - 0.92*	*1530*
13	*700*	*Incompressible*	*Case 1*	*0.532*	*15690*
14	*700*	*Incompressible*	*Case 2*	*0.532*	*1020*
15	*700*	*Incompressible*	*Case 3*	*0.532*	*890*
16	*700*	*Compressible*	*Case 1*	*0.48 - 0.55*	*15860*
17	*700*	*Compressible*	*Case 2*	*0.53 - 0.54*	*1030*
18	*700*	*Compressible*	*Case 3*	*0.53 - 0.54*	*890*
19	*1400*	*Incompressible*	*Case 2*	*1.104*	*3190*
20	*1400*	*Incompressible*	*Case 2*	*0.532*	*741*
21	*1400*	*Compressible*	*Case 2*	*1.13 - 1.16*	*2740*
22	*1400*	*Compressible*	*Case 2*	*0.53 - 0.54*	*590*

Table A.2: All simulations done with small-scale conditions corresponding to previous experimental conditions with solver, case, velocity and resulting pressure.

Simulation	***Solver***	***Case***	***U* [*m/s*]**	***P* [*Pa*]**
1	*Incompressible*	*Case 1*	*0.29*	*7190*
2	*Incompressible*	*Case 2*	*0.88*	*4235*
3	*Incompressible*	*Case 3*	*1.02*	*5000*
4	*Compressible*	*Case 1*	*0.24*	*5060*
5	*Compressible*	*Case 2*	*0.74*	*3020*
6	*Compressible*	*Case 3*	*0.86*	*3560*

B Geometry of Upscaled Simulations with Furnace Conditions

```
/*--------------------------------*- C++ -*----------------------------------*\
  =========                 |
  \\      /  F ield         | OpenFOAM: The Open Source CFD Toolbox
   \\    /   O peration     | Website:  https://openfoam.org
    \\  /    A nd           | Version:  9
     \\/     M anipulation  |
\*---------------------------------------------------------------------------*/
FoamFile
{
    format      ascii;
    class       dictionary;
    object      blockMeshDict;
}
// * * * * * * * * * * * * * * * * * * * * * * * * * * * * * * * * * * * * * //


convertToMeters 0.001;

angle 0;

width     500;
lenInlet  1;
lenPoro   1500;
lenOutlet 1;

yCells      30;
zCells      1;
nInletCells  1;
nPoroCells   600;
nOutletCells 1;

vertices #codeStream
{
    codeInclude
    #{
        #include "pointField.H"
    #};

    code
    #{
        const scalar halfWidth = ($width)/2.0;

        // Length between the bend and outlet
        const scalar distOutlet = $lenPoro + $lenOutlet;

        pointField points
        ({
            point(0,          0,      -halfWidth), // pt 0
            point($lenPoro,   0,      -halfWidth), // pt 1
            point(distOutlet, 0,      -halfWidth), // pt 2
            point(0,          $width, -halfWidth), // pt 3
            point($lenPoro,   $width, -halfWidth), // pt 4
            point(distOutlet, $width, -halfWidth)  // pt 5
        });



        // Append points 6 and 7
        points.append(points[0]);  // pt 6
        points.append(points[3]);  // pt 7

        points[6].x() = -$lenInlet;
        points[7].x() = -$lenInlet;

        // Duplicate z points
        points.append(cmptMultiply(points, vector(1, 1, -1)));
```

```
        os  << points;
    #};
};

blocks
(
    // Inlet block
    hex (6 0 3 7 14 8 11 15)
    inlet  ($nInletCells $yCells $zCells) simpleGrading (1 1 1)

    // Porosity block
    hex (0 1 4 3 8 9 12 11)
    porosity ($nPoroCells $yCells $zCells) simpleGrading (1 1 1)

    // Outlet block
    hex (1 2 5 4 9 10 13 12)
    outlet ($nOutletCells $yCells $zCells)  simpleGrading (1 1 1)
);

defaultPatch
{
    name walls;
    type wall;
}

boundary
(
    porosityWall
    {
        type wall;
        faces
        (
            (8 9 12 11)
            (0 3 4 1)
            (0 1 9 8)
            (3 11 12 4)
        );
    }

    inlet
    {
        type patch;
        faces
        (
            (14 15 7 6)
        );
    }

    outlet
    {
        type patch;
        faces
        (
            (2 5 13 10)
        );
    }
);

// ************************************************************************* //
```

C Geometry of Small-Scale Cold Experiment

```
*---------------------------------*- C++ -*----------------------------------*\
  =========                 |
  \\      /  F ield         | OpenFOAM: The Open Source CFD Toolbox
   \\    /   O peration     | Website:  https://openfoam.org
    \\  /    A nd           | Version:  9
     \\/     M anipulation  |
\*---------------------------------------------------------------------------*/
FoamFile
{
    format      ascii;
    class       dictionary;
    object      blockMeshDict;
}
// * * * * * * * * * * * * * * * * * * * * * * * * * * * * * * * * * * * * * * * //


convertToMeters 0.001;

angle 0;

width     185;
lenInlet  30;
lenPoro   700;
lenOutlet 10;

yCells      20;
zCells      1;
nInletCells  5;
nPoroCells   300;
nOutletCells 5;

vertices #codeStream
{
    codeInclude
    #{
        #include "pointField.H"
    #};

    code
    #{
        const scalar halfWidth = ($width)/2.0;

        // Length between the bend and outlet
        const scalar distOutlet = $lenPoro + $lenOutlet;

        pointField points
        ({
            point(0,          0,      -halfWidth), // pt 0
            point($lenPoro,   0,      -halfWidth), // pt 1
            point(distOutlet, 0,      -halfWidth), // pt 2
            point(0,          $width, -halfWidth), // pt 3
            point($lenPoro,   $width, -halfWidth), // pt 4
            point(distOutlet, $width, -halfWidth)  // pt 5
        });



        // Append points 6 and 7
        points.append(points[0]);  // pt 6
        points.append(points[3]);  // pt 7

        points[6].x() = -$lenInlet;
        points[7].x() = -$lenInlet;

        // Duplicate z points
        points.append(cmptMultiply(points, vector(1, 1, -1)));
```

```
        os  << points;
    #};
};

blocks
(
    // Inlet block
    hex (6 0 3 7 14 8 11 15)
    inlet  ($nInletCells $yCells $zCells) simpleGrading (1 1 1)

    // Porosity block
    hex (0 1 4 3 8 9 12 11)
    porosity ($nPoroCells $yCells $zCells) simpleGrading (1 1 1)

    // Outlet block
    hex (1 2 5 4 9 10 13 12)
    outlet ($nOutletCells $yCells $zCells)  simpleGrading (1 1 1)
);

defaultPatch
{
    name walls;
    type wall;
}

boundary
(
    porosityWall
    {
        type wall;
        faces
        (
            (8 9 12 11)
            (0 3 4 1)
            (0 1 9 8)
            (3 11 12 4)
        );
    }

    inlet
    {
        type patch;
        faces
        (
            (14 15 7 6)
        );
    }

    outlet
    {
        type patch;
        faces
        (
            (2 5 13 10)
        );
    }
);

// ************************************************************************* //
```

Astrid Nordhus

Modelling Gas Flow in Furnaces for Si Production

NTNU
Norwegian University of
Science and Technology